

---

# Multi-physics Simulation Guided Generative Diffusion Models with Applications in Fluid and Heat Dynamics

---

Naichen Shi<sup>1</sup> Hao Yan<sup>2</sup> Shenghan Guo<sup>2</sup> Raed Al Kontar<sup>1</sup>

## Abstract

In this paper, we present a generic physics-informed generative model called MPDM that integrates multi-fidelity physics simulations with diffusion models. MPDM categorizes multi-fidelity physics simulations into inexpensive and expensive simulations, depending on computational costs. The inexpensive simulations, which can be obtained with low latency, directly inject contextual information into DDMs. Furthermore, when results from expensive simulations are available, MPDM refines the quality of generated samples via a guided diffusion process. This design separates the training of a denoising diffusion model from physics-informed conditional probability models, thus lending flexibility to practitioners. MPDM builds on Bayesian probabilistic models and is equipped with a theoretical guarantee that provides upper bounds on the Wasserstein distance between the sample and underlying true distribution. The probabilistic nature of MPDM also provides a convenient approach for uncertainty quantification in prediction. Our models excel in cases where physics simulations are imperfect and sometimes inaccessible. We use a numerical simulation in fluid dynamics and a case study in heat dynamics within laser-based metal powder deposition additive manufacturing to demonstrate how MPDM seamlessly integrates multi-fidelity physics simulations and observations to obtain surrogates with superior predictive performance.

details. At the heart of these generative models are score-based *denoising diffusion models* (DDMs) designed to learn complex statistical patterns from high-dimensional training data (Ho et al., 2020). The flexible sampling procedure of DDMs allows for integrating prompts into the denoising process to generate controllable and customized samples (Chen et al., 2023).

Despite the success of DDMs in photo and video synthesis, two challenges hinder their application in engineering fields. First, the predictions generated by standard DDMs may not consistently align with the laws of physics. For example, even state-of-the-art DDMs like SORA can misinterpret physical interactions in the real world, generating videos that contain artifacts and lack long-term consistency. Second, DDMs are often data-hungry. To understand the detailed patterns in images, modern DDMs may need more than thousands of millions of training samples (Ramesh et al., 2022). This demand for large data limits the applicability of generative models in environments where acquiring high-quality and large-scale datasets is challenging or prohibitively expensive.

Alternative solutions to pure data-driven statistical modeling exist. In the field of science and engineering, researchers and practitioners often possess domain expertise in physical knowledge that reflects underlying laws governing dynamic systems of interest. Thus, a natural strategy is to embed such physical knowledge into generative models. Indeed, in natural language processing (Liu et al., 2023) and retrieval-augmented generation (Lewis et al., 2020), a similar technique that combines factual knowledge with language generation, is prevalently applied (Lewis et al., 2020).

In the literature, two types of research areas are proposed to integrate physical knowledge into deep learning models. 1) **Physics-Informed Neural Networks (PINNs)**: PINNs learn the solution of a set of ordinary differential equations (ODEs) or partial differential equations (PDEs) by using neural networks (NNs), ensuring that the network’s predictions are consistent with known physical principles. This approach typically involves incorporating differential equations that describe physical systems into the loss function of the NN (Cuomo et al., 2022). Along this line of research,

## 1. Introduction

The era of generative AI is unfolding. Denoising diffusion process-based deep generative models, such as SORA (OpenAI, 2024), Midjourney (Midjourney, 2024), and Stable diffusion (Stability AI, 2024), can generate photorealistic and aesthetically pleasing images and videos with vivid

---

<sup>1</sup> University of Michigan <sup>2</sup> Arizona State University. Correspondence to: Raed Al Kontar <alkontar@umich.edu>.

neural operators are designed to learn the nonlinear operators dictated by physical principles (Lu et al., 2021; Li et al., 2020; Kovachki et al., 2023). However, typical PINNs assume that the physical law is an accurate representation of the underlying system (Raissi et al., 2017; 2019). 2) **Physics-Constrained Neural Networks (PCNNs)**: PCNNs focus on enforcing physical or other knowledge constraints during the training process (Zhu et al., 2019; Sun & Wang, 2020; Zhang et al., 2020). This can be achieved by adding regularization terms to the loss function, which penalizes deviations from known physical behaviors. Such constraints guide the learning process, ensuring that the resulting model adheres to physical principles. Along this line, there has been work on extending the constraints to Bayesian NNs to model and infer uncertainty in the data (Yang et al., 2020; Huang et al., 2023). PCNNs are particularly useful when dealing with limited or noisy data, as the physical constraints help to regularize the learning process and prevent overfitting. However, the penalty approach also requires careful selection of the tuning parameters and assumes that the PDEs that characterize the evolution of the dynamic system are accurate to some degree.

Despite the popularity of the models above, their outputs are vulnerable to model misspecifications because we rarely can easily model the exact underlying physics accurately or within a reasonable timeframe, especially for very complex processes commonly observed in engineering systems (see Section 6). Instead, in many practical applications, physical knowledge is often implemented by computer simulators. Indeed, in recent decades, there has been remarkable progress in computer simulators for diverse systems, such as computational biology (Thieme, 2018), material science (Fonseca Guerra et al., 1998), and quantum systems (Karsch, 2002).

In this paper, we specifically focus on the outputs of such simulators. Our overarching goal is to effectively fuse these outputs with real observations using DDMs to obtain improved surrogates capable of quantifying uncertainty. A straightforward strategy is to use simulation outputs as additional inputs to the denoising neural network (DeNN) employed in the reverse diffusion process in DDMs. During the training stage, DeNNs are trained to gradually denoise corrupted samples under the guidance of physics simulations. The trained DeNNs then generate samples with the help of physics simulations in the inference stage.

Though intuitive and easy to implement, this approach has a critical caveat regarding computational costs. High-fidelity simulations require significant computing resources, such as modern numerical weather prediction programs, which use up to  $10^{15}$  floating-point operations per second (Benjamin et al., 2019). Simulators with lower computational demands can be available but often at the cost of worse

performance (Lam et al., 2023). This trade-off between resources and performance is common across fields. A relevant example is that for PDE solvers, higher resolution grids improve accuracy but increase storage and computation costs (Gramacy, 2020). Consequently, depending on the computational demands and resources available, results from expensive simulation programs may not be accessible in large scales.

Therefore, training data-hungry DeNNs on these results may not be feasible. We thus propose an alternative approach to leverage the information from the potentially sparse simulation results. The method is inspired by conditional DDMs (Song et al., 2021b): instead of using expensive simulations as input, we use them to refine the sampling trajectory at the inference stage of the DDM. This strategy builds on Bayesian inference, which effectively borrows information from expensive simulations without retraining DeNNs.

Namely, we develop a general-purpose multi-physics guided diffusion model (MPDM), a framework that integrates multiple computer simulation models into DDMs. In MPDM, we categorize physical simulators into two classes: inexpensive simulators, whose results are easily obtainable with low latency, and expensive simulators, which output results with higher fidelity but consume larger computational resources. We design separate knowledge integration techniques for different simulators. More specifically, we use inexpensive computer simulations as additional inputs to the DeNN, which is trained to generate predictions with insights from simulations. For the expensive computer simulations, we construct a separate conditional probability model and use a conditional diffusion process to further improve the sampling quality. The design of MPDM decouples the training of probabilistic models for different physics simulators, facilitating its implementation in practice, especially when some simulation results are not always available.

The proposed MPDM is a hybrid of physics-based computer simulations and data-driven DDMs, thus reaping advantages from both worlds. The model becomes a physics-informed surrogate (Gramacy, 2020) that inherits physics knowledge from simulations while learning statistical patterns from data. As a result, the generated predictions can abide by the principles of physics while remaining consistent with the observations.

We highlight several benefits of MPDM in the following,

- *Generality*: MPDM operates on the outputs of simulators rather than specific forms of ODEs or PDEs. Thus, MPDM can work with a wide range of physics simulators, even if the simulators are black-box functions for practitioners.
- *Flexibility*: The conditional probability models for dif-

ferent physics simulators can be trained separately. Such a decoupled design provides an interface that allows for easy plug-ins of the results from different simulators.

- *Computational efficiency*: Unlike physics surrogates implemented by Gaussian processes (GPs) (Gramacy, 2020), whose computation complexity often scales quadratically or even cubically with the training dataset size (Williams & Rasmussen, 2006), the inference time complexity of MPDM is independent of the training dataset size. Additionally, the DeNN in MPDM shows strong performance in modeling high-dimensional data.
- *Uncertainty quantification*: By initializing the reverse diffusion from different Gaussian random vectors, MPDM can naturally construct confidence intervals that characterize predictive uncertainties.
- *Theory*: MPDM is inspired by Bayes law and stochastic dynamics of reverse diffusion processes. We prove that, in the continuous limit, the Wasserstein distance between the sample distribution and the ground-truth conditional distribution is upper bounded by statistical errors.

We demonstrate the capability of MPDM on two exemplary applications: a *fluid system* and a *thermal process* from additive manufacturing, each representing different types of physics simulations. In the fluid system, we leverage outputs from existing computational fluid dynamics (CFD) programs with varying levels of fidelity to predict the future evolution of the buoyancy of fumes. Additionally, in a real case study of an additive manufacturing thermal process, we implement ad-hoc PDE simulators. Both applications illustrate how MPDM integrates statistical knowledge from real observations with physics knowledge from simulations to better predict the evolution of physical systems. The code to reproduce numerical results in this paper is available in the repository <https://github.com/UMDataScienceLab/MGDM>.

## 2. Related work

This section delves into recent advancements and applications of DDMs, particularly in the context of video generation and integration of physics simulations. We introduce the basics of DDMs, their conditional and constrained counterparts, the use of physics surrogates to enhance performance, and the embedding of physics knowledge into the diffusion process to highlight our framework’s methodology and benefits.

**Diffusion and video generation** DDMs (Ho et al., 2020) introduce a flexible and expressive framework for generative

models. The connections between DDMs, score matching, and stochastic differential equations are explored in a series of works (Song et al., 2020; Song & Ermon, 2019; Song et al., 2021a). As discussed, DDMs form the backbone of multiple modern large-scale generative models (OpenAI, 2024; Midjourney, 2024; Stability AI, 2024).

In the temporal data generation domain, DDM and its variants can effectively model temporal interactions in multivariate time series (Li et al., 2022; Kolloviev et al., 2024) and video frames (Ho et al., 2022a;b). Our work also predicts temporal evolutions of dynamic systems, but under the guidance of physics simulations.

**Conditional diffusion** Recent methods have been proposed to leverage the information from external conditions to guide diffusion processes (Chung et al., 2023; Yang et al., 2023; Chung et al., 2024). A well-known example of this practice is the use of spectral signals in the frequency domain to inform Magnetic Resonance Imaging (MRI) reconstruction (Jalal et al., 2021; Song et al., 2021b). In video generation, motion vectors can also guide the spatial and temporal evolution of frames (Wang et al., 2024). Modern video generative models often condition on input texts as well (Chen et al., 2023; OpenAI, 2024). With a similar rationale, we condition on physics simulators to guide DDMs.

**Physics-informed surrogates** Research that aims to combine statistical models with physics knowledge has a long history. One prominent method, proposed by Kennedy and O’Hagan (KOH) (Kennedy & O’Hagan, 2001; 2000), predicts the discrepancy between physics simulations and real-life observations by using GPs and employs a Bayesian calibration approach to optimize the parameters. In the literature of experimental design, such statistical models that emulate physics observations or computer simulations are often called surrogate models (Gramacy, 2020). Many surrogate models build on GPs (Mak et al., 2018; Ji et al., 2023; Swiler et al., 2020; Spitieris & Steinsland, 2023). However, the application of GPs in large-scale and high-dimensional datasets is limited as computation costs increase with training dataset size (Williams & Rasmussen, 2006). Our proposed model MPDM circumvents the issue by using DDMs.

**Physics-driven diffusion** A few recent works propose to bring physics knowledge into DDMs (Shu et al., 2023; Jacobsen et al., 2023). Among them, CoCoGen (Jacobsen et al., 2023) enforces PDE constraints onto the reverse diffusion process, which improves the performance of Darcy flow modeling. However, in broader applications, imposing PDE constraints can be too restrictive and exacerbate modeling bias (Gramacy, 2020). (Shu et al., 2023) uses residuals of the PDE as additional inputs to the denoising

network and achieves remarkable performance in fluid field super-resolution. Despite the success, it is uneasy to apply the method in (Shu et al., 2023) to applications where the physics cannot be described by a single PDE. Unlike these approaches, our method MPDM does not require the knowledge of the underlying PDE. As long as practitioners have access to the outputs of physics simulators, they can use the outputs to guide their DDMs. Hence, the requirement for domain knowledge is minimized. Additionally, since the MPDM is trained on real observations, the statistical knowledge from data can be leveraged to improve the results from potentially biased physics simulations. The two applications in this paper demonstrate the bias-mitigation effect.

**Constrained diffusion** Constrained DDMs have been extensively studied to understand how physical constraints influence the training process of DDMs. These studies reveal that incorporating physical constraints, such as boundaries or barriers, significantly alters diffusion dynamics compared to unrestricted environments. Recent advancements include DDMs on Riemannian manifolds (De Bortoli et al., 2022; Huang et al., 2022), investigating the diffusion dynamics on Riemannian manifolds, and DDMs on constrained domains (Fishman et al., 2023), introducing the logarithmic barrier metric and reflected Brownian motion, demonstrating practical utility in fields like robotics and protein design. Constrained DDMs have found applications in robotics (Urain et al., 2023) and crystal structure prediction (Jiao et al., 2024). However, these methods often assume that the constrained domain for the DDMs is known, which is challenging to determine in complex real-world systems.

### 3. Model

In this section, we progressively construct models that fuse knowledge from multiple physics simulators into DDMs. The overarching goal is to predict the evolution of dynamical systems to high fidelity and verisimilitude with historical observations and access to physics simulations. We use a vector  $\mathbf{x}_{0,s}$  to represent the state of the system at time  $s$ , where the subscript 0 denotes the real-life observed data.

As discussed, we group multi-fidelity physical simulators into two categories: inexpensive and expensive simulations. We assume practitioners can call inexpensive simulators at each time step  $s$  at low latency. The result is denoted as a vector  $\mathbf{c}_{1,s}$ . Expensive physics simulations are more time-consuming and may not be accessible at all time. We use a vector  $\mathbf{c}_{2,s}$  to denote the result of expensive simulation at time  $s$ , *if available*.  $\mathbf{c}_{1,s}$  and  $\mathbf{c}_{2,s}$  can incorporate a broad range of computer simulations or statistical surrogates (Gramacy, 2020).

In the rest of this section, we will first review the DDM

framework with a focus on denoising diffusion implicit models (DDIMs) (Song et al., 2020), an instance of DDMs popular in the field of image and video generation (Rombach et al., 2022; Yang et al., 2023). We will then develop techniques to incorporate the results from both inexpensive and expensive computer simulations. Finally, we will present the pseudocode for our training and sampling algorithms.

#### 3.1. Standard diffusion model

Denoising Diffusion Implicit Models (DDIMs) use a series of Gaussian noise with increasing variance to corrupt the data, then train DeNNs to gradually reconstruct clean data from corrupted ones. The DDIM consists of multiple steps  $t = 0, 1, 2, \dots, T$  (Ho et al., 2020), each one of which corresponds to a specific level of variance in the Gaussian noise. For clarity, we use  $\mathbf{x}_{t,s}$  to denote the step- $t$  diffusion of the state vector observed at time  $s$ . It is important to note that  $t$  signifies the diffusion step, whereas  $s$  indicates the actual time within the dynamic system. Fig. 1 provides a pictorial depiction of this process, illustrating both the diffusion mechanism and the temporal evolution of data.

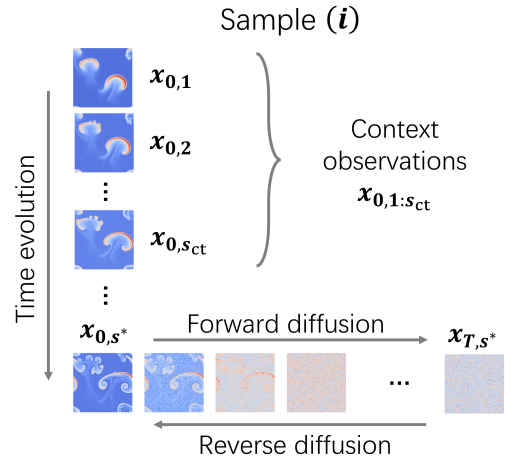


Figure 1. An illustration of the time evolution of dynamic systems and the diffusion process. In the forward diffusion process, Gaussian noises with increasing variance gradually corrupt data  $\mathbf{x}_{0,s^*}$  into almost white noise  $\mathbf{x}_{T,s^*}$ . The reverse diffusion process removes noise and restores clean samples.

In DDIM, the forward diffusion process is given as,

$$\mathbf{x}_{t,s} = \sqrt{1 - \beta_t} \mathbf{x}_{t-1,s} + \sqrt{\beta_t} \mathbf{z}_{t,s}, \quad (1)$$

where  $\mathbf{z}_{t,s}$  are i.i.d. Gaussian noise vectors and  $\beta_t$  is a predefined constant that determines the noise variances. Similar to Ho et al. (2020), we introduce notation  $\alpha_t = 1 - \beta_t$  and  $\bar{\alpha}_t = \prod_{\tau=1}^t \alpha_\tau$ .

In the continuous limit, the forward diffusion process (1) reduces to a stochastic differential equation (SDE) (Song &

Ermon, 2019),

$$d\mathbf{x}_{t,s} = -\frac{\beta_t}{2}\mathbf{x}_{t,s}dt + \sqrt{\beta_t}d\mathbf{w}_t, \quad (2)$$

where  $\mathbf{w}_t$  is the standard Brownian motion or Weiner process. With a slight abuse of notation, the subscript  $t$  denotes a continuous variable in (2) and a discrete variable in (1). In literature, (2) is often called a variance-preserving SDE (Song & Ermon, 2019).

In the task of future physics state prediction, historic observations are often available to practitioners. We use  $s_{\text{ct}}$  to denote the number of context (already observed) observations, and  $\mathbf{x}_{0,1:s_{\text{ct}}}$  as a shorthand notation for the concatenated observed vector  $[\mathbf{x}_{0,1}, \mathbf{x}_{0,2}, \dots, \mathbf{x}_{0,s_{\text{ct}}}]$  (see Time evolution in Fig. 1). Mathematically, the task can be formulated as predicting/sampling the state vector  $\mathbf{x}_{0,s^*}$  at a time of interest  $s^*$  from the predictive distribution  $p(\mathbf{x}_{0,s^*}|\mathbf{x}_{0,1:s_{\text{ct}}})$ , where  $s_{\text{ct}} < s^*$ . The target distribution  $p(\mathbf{x}_{0,s^*}|\mathbf{x}_{0,1:s_{\text{ct}}})$  is a conditional distribution of future state vector  $\mathbf{x}_{0,s^*}$  given the observed state vectors  $\mathbf{x}_{0,1:s_{\text{ct}}}$ .

It is important to note that for predictions at multiple future time points, or multiple values of  $s^*$ , practitioners can efficiently apply the DDM framework by simply stacking these state vectors and sampling from the the distribution of stacked vectors. Hence, for simplicity and without any loss of generality, we use  $\mathbf{x}_{0,s^*}$  to signify the state vector at any given target time  $s^*$ . Typically in autoregressive tasks,  $s^*$  is set to  $s_{\text{ct}} + 1$ .

To generate high-quality samples, DDMs exploit an existing dataset  $\mathcal{D} = \{(\mathbf{x}_{0,1:s_{\text{ct}}}^{(i)}, \mathbf{x}_{0,s^*}^{(i)})\}_{i=1}^N$  to learn the target conditional distribution, where the superscript  $(i)$  is the observation index. Different  $i$  denotes different collected evolution trajectories of state vectors.  $N$  is the total number of trajectories in the training set.

We briefly describe the training objective of DDIM. By iteratively applying (1), one can show that  $\mathbf{x}_{t,s}$  has the same distribution as  $\sqrt{\alpha_t}\mathbf{x}_{0,s^*} + \sqrt{1-\alpha_t}\boldsymbol{\epsilon}$  where  $\boldsymbol{\epsilon}$  is a vector whose elements are i.i.d. standard Gaussians. DDIM leverages such fact to train an iterative DeNN  $\epsilon_\theta(\cdot)$  that predicts the noise  $\boldsymbol{\epsilon}$  from the corrupted sample  $\mathbf{x}_{t,s^*}$ . More specifically, the training objective of DDIM is,

$$\min_{\theta} \mathbb{E}_{(\mathbf{x}_{0,s^*}, \mathbf{x}_{0,1:s_{\text{ct}}}) \sim \mathcal{D}, t \sim \mathcal{U}[0, T], \boldsymbol{\epsilon} \sim \mathcal{N}(0, \mathbf{I})} \left[ \left\| \boldsymbol{\epsilon} - \epsilon_\theta(\sqrt{\alpha_t}\mathbf{x}_{0,s^*} + \sqrt{1-\alpha_t}\boldsymbol{\epsilon}, t, \mathbf{x}_{0,1:s_{\text{ct}}}) \right\|^2 \right]. \quad (3)$$

In (3), the diffusion and denoising only happen at the target time  $s^*$ . The objective is to minimize the difference between the noise added to the sample and the noise predicted by the denoising network. It is worth noting that theoretically, the denoising objective (3) is related to the score

function in statistics: roughly speaking, if the sample size goes to infinity and (3) is exactly minimized, the optimal  $\epsilon_\theta^*$  becomes (Song & Ermon, 2019),

$$\epsilon_\theta^*(\mathbf{x}_{t,s}, t, \mathbf{x}_{0,1:s_{\text{ct}}}) = -\sqrt{1-\alpha_t}\nabla_{\mathbf{x}_{t,s}} \log p(\mathbf{x}_{t,s^*}|\mathbf{x}_{0,1:s_{\text{ct}}}), \quad (4)$$

where  $p(\mathbf{x}_{t,s^*}|\mathbf{x}_{0,1:s_{\text{ct}}})$  is the p.d.f. of the random vector  $\mathbf{x}_{t,s^*} = \sqrt{\alpha_t}\mathbf{x}_{0,s^*} + \sqrt{1-\alpha_t}\boldsymbol{\epsilon}$ , and the score function is the gradient of the logarithm of the p.d.f.

In the inference stage, DDIM (Song et al., 2020) generates high-quality samples from the approximated score functions. More precisely, DDIM samples  $\mathbf{x}_{T,s^*}$  from the standard normal distribution, then applies the denoising network  $\epsilon_\theta$  to iteratively denoise  $\mathbf{x}_{t,s^*}$ :

$$\mathbf{x}_{t-1,s^*} = \frac{1}{\sqrt{\alpha_t}} \left( \mathbf{x}_{t,s^*} - \frac{(1-\alpha_t)\epsilon_\theta(\mathbf{x}_{t,s^*}, t, \mathbf{x}_{0,1:s_{\text{ct}}})}{\sqrt{1-\alpha_t} + \sqrt{\alpha_t - \bar{\alpha}_t}} \right), \quad (5)$$

for  $t$  from  $T$  to 1. The coefficient  $\frac{1-\alpha_t}{\sqrt{1-\alpha_t} + \sqrt{\alpha_t - \bar{\alpha}_t}}$  will converge to  $\frac{\beta_t}{2\sqrt{1-\alpha_t}}$  when  $\beta_t$  is small. We obtain  $\mathbf{x}_{0,s^*}$  eventually.

From the perspective of SDEs, if the denoising network is properly trained as in (4), the sampling rule (5) is a discretized version of the reverse process ODE (2),

$$d\mathbf{x}_{t,s^*} = \left( \frac{\beta_t\mathbf{x}_{t,s^*}}{2} + \frac{\beta_t}{2}\nabla_{\mathbf{x}_{t,s^*}} \log p(\mathbf{x}_{t,s^*}|\mathbf{x}_{0,1:s_{\text{ct}}}) \right) dt, \quad (6)$$

Under the dynamics specified by (6), the random vector  $\mathbf{x}_{0,s^*}$  will follow the desired predictive distribution  $p(\mathbf{x}_{0,s^*}|\mathbf{x}_{0,1:s_{\text{ct}}})$  if properly initialized. Such connection justifies (5) theoretically (Song et al., 2020).

### 3.2. Inexpensive physics-conditioned diffusion

As discussed, the training objective (3) and sampling scheme (5) (or the continuous version (6)) only focus on the statistical patterns in the data and can overlook the physics mechanisms, especially when the size of the training dataset  $\mathcal{D}$  is not extremely large. Physics simulations can help alleviate the issue. We assume that simulations can make predictions about the future evolution of the system. The output at time  $s$  is  $\mathbf{c}_{1,s}$ . We further assume here that the physics simulations are inexpensive, allowing simulation predictions to be obtained for each sample in the training and sampling stages with low latency.

With the physics simulator, we can build an augmented training dataset by combining the training data and inexpensive simulation data at target time  $s^*$ ,  $\mathcal{D}_{\text{aug}} = \{(\mathbf{x}_{0,s^*}^{(i)}, \mathbf{x}_{0,1:s_{\text{ct}}}^{(i)}, \mathbf{c}_{1,s^*}^{(i)})\}_{i=1}^N$ . The augmented dataset enables us to train a conditional diffusion network  $\epsilon_\theta(\cdot)$  that

takes not only the initial frames  $\mathbf{x}_{0,1:s_{\text{ct}}}$  but also the simulation prediction  $\mathbf{c}_{1,s^*}$  as its contextual input.

The training objective of the inexpensive physics-conditioned diffusion model thus becomes

$$\min_{\theta} \mathbb{E}_{(\mathbf{x}_{0,s^*}, \mathbf{x}_{0,1:s_{\text{ct}}}, \mathbf{c}_{1,s^*}) \sim \mathcal{D}_{\text{aug}}, t \sim \mathcal{U}[0, T], \epsilon \sim \mathcal{N}(0, \mathbf{I})} \left[ \left\| \epsilon - \epsilon_{\theta}(\sqrt{\alpha_t} \mathbf{x}_{0,s^*} + \sqrt{1 - \alpha_t} \epsilon, t, \mathbf{x}_{0,1:s_{\text{ct}}}, \mathbf{c}_{1,s^*}) \right\|^2 \right]. \quad (7)$$

Similar to DDIM, we use Monte Carlo approximation to minimize the objective. The pseudocode is presented in Algorithm 2.

Intuitively, the physics context  $\mathbf{c}_{1,s^*}$  can bring additional physics knowledge to the model, thus augmenting the authenticity of the prediction. The denoising network  $\epsilon_{\theta}$  is then trained to absorb such physics knowledge. Such intuition is corroborated by our theoretical analysis in Theorem 4.1 (see Section 4).

Accordingly, the iterative sampling rule becomes,

$$\mathbf{x}_{t-1,s^*} = \frac{1}{\sqrt{\alpha_t}} \left( \mathbf{x}_{t,s^*} - \frac{(1 - \alpha_t) \epsilon_{\theta}(\mathbf{x}_{t,s^*}, t, \mathbf{x}_{0,1:s_{\text{ct}}}, \mathbf{c}_{1,s^*})}{\sqrt{1 - \bar{\alpha}_t} + \sqrt{\alpha_t - \bar{\alpha}_t}} \right), \quad (8)$$

for  $t$  from  $T$  to 1, starting from  $\mathbf{x}_{T,s^*} \sim \mathcal{N}(0, \mathbf{I})$ .

The sampling rule (8) is analogous to that in (5). The only difference is that we augment the input to the DeNN with the predictions from the physics simulations. We also provide a pseudocode of the sampling rule as the choice 1 of Algorithm 3. Our experiments show that the augmented information can significantly improve the sampling performance.

### 3.3. Expensive physics-conditioned diffusion

Clearly, the approach above is simple since simulations are cheap, but what if we have simulations that are expensive? Often, practitioners can obtain physics predictions from more expensive but potentially more accurate physics models. We denote the results from an expensive simulator at time  $s^*$  as  $\mathbf{c}_{2,s^*}$ . Then, an augmented dataset of trajectories and simulations is  $\{\mathbf{x}_{0,s^*}^{(i)}, \mathbf{x}_{0,1:s_{\text{ct}}}^{(i)}, \mathbf{c}_{1,s^*}^{(i)}, \mathbf{c}_{2,s^*}^{(i)}\}_{i=1}^N$ . However, due to high computation costs or latency, we assume that  $\mathbf{c}_{2,s^*}^{(i)}$  may only be available for a subset of  $i \in \mathcal{S}_{\text{available}}$ . Thus, we cannot directly feed  $\mathbf{c}_{2,s^*}$  into the DeNN. This section employs a different strategy to handle the case where  $\mathbf{c}_{2,s^*}^{(i)}$  is available. Here, we leverage conditional DDMs to guide the diffusion process by both inexpensive and expensive simulators, namely,  $p(\mathbf{x}_{0,s^*} | \mathbf{c}_{1,s^*}, \mathbf{c}_{2,s^*})$ . Notably, our method exploits the sparsely available  $\mathbf{c}_{2,s^*}$ , decoupled from the training procedure in Section 3.2, ensuring that

the unavailability of  $\mathbf{c}_{2,s^*}^{(i)}$  does not affect the training of the denoising network  $\epsilon_{\theta}$ .

We motivate our derivation from the reverse diffusion ODE,

$$d\mathbf{x}_{t,s^*} = \frac{\beta_t}{2} (\mathbf{x}_{t,s^*} + \nabla_{\mathbf{x}_{t,s^*}} \log p(\mathbf{x}_{t,s^*} | \mathbf{x}_{0,1:s_{\text{ct}}}, \mathbf{c}_{1,s^*}, \mathbf{c}_{2,s^*})) dt. \quad (9)$$

One can see that the conditional score function  $\nabla_{\mathbf{x}_{t,s^*}} \log p(\mathbf{x}_{t,s^*} | \mathbf{x}_{0,1:s_{\text{ct}}}, \mathbf{c}_{1,s^*}, \mathbf{c}_{2,s^*})$  replaces its counterpart in (6) and plays the central role in the reverse diffusion process. Therefore, it suffices to derive an estimate of the conditional score function.

From the Bayes's rule, we know for any  $t \geq 0$ ,

$$\begin{aligned} \nabla \log p(\mathbf{x}_{t,s^*} | \mathbf{c}_{1,s^*}, \mathbf{c}_{2,s^*}) \\ = \nabla \log p(\mathbf{x}_{t,s^*} | \mathbf{c}_{1,s^*}) + \nabla \log p(\mathbf{c}_{2,s^*} | \mathbf{x}_{t,s^*}, \mathbf{c}_{1,s^*}). \end{aligned}$$

The first term can be approximated by the denoising network trained by Algorithm 2. We use  $\mathbf{g}(\mathbf{x}_{0,1:s_{\text{ct}}}, \mathbf{c}_{2,s^*}, \mathbf{c}_{1,s^*}, t)$  to denote an estimate of the second term,

$$\mathbf{g}(\mathbf{x}_{0,1:s_{\text{ct}}}, \mathbf{c}_{1,s^*}, \mathbf{c}_{2,s^*}, t) \approx \nabla_{\mathbf{x}_{t,s^*}} \log p(\mathbf{c}_{2,s^*} | \mathbf{x}_{t,s^*}, \mathbf{c}_{1,s^*}). \quad (10)$$

In literature, there are multiple ways to construct estimates for  $\mathbf{g}$ . When the conditional probability  $p(\mathbf{c}_{2,s^*} | \mathbf{x}_{0,s^*}, \mathbf{c}_{1,s^*})$  is known, we introduce a conceptually simple and computationally tractable procedure inspired by (Chung et al., 2023). The pseudocode is presented in Algorithm 1.

---

**Algorithm 1** Estimate the gradient of the log conditional probability  $\nabla_{\mathbf{x}_{t,s^*}} \log p(\mathbf{c}_{2,s^*} | \mathbf{x}_{t,s^*}, \mathbf{c}_{1,s^*})$

---

- 1: Input the conditional distribution  $p(\mathbf{c}_{2,s^*} | \mathbf{x}_{0,s^*}, \mathbf{c}_{1,s^*})$ ,
  - 2: Estimate  $\hat{\mathbf{x}}_{0,s^*}, \theta(\mathbf{x}_{t,s^*}, \mathbf{c}_{1,s^*}, t) = \frac{\mathbf{x}_{t,s^*} - \sqrt{1 - \bar{\alpha}_t} \epsilon_{\theta}(\mathbf{x}_{t,s^*}, \mathbf{c}_{1,s^*}, t)}{\sqrt{\alpha_t}}$ ,
  - 3: Calculate  $\nabla_{\hat{\mathbf{x}}_{0,s^*}, \theta} \log p(\mathbf{c}_{2,s^*} | \hat{\mathbf{x}}_{0,s^*}, \theta, \mathbf{c}_{1,s^*})$ ,
  - 4: Take  $\mathbf{g} = \frac{1}{\sqrt{\alpha_t}} \nabla_{\hat{\mathbf{x}}_{0,s^*}, \theta} \log p(\mathbf{c}_{2,s^*} | \hat{\mathbf{x}}_{0,s^*}, \theta, \mathbf{c}_{1,s^*})$ .
  - 5: Return  $\mathbf{g}$ .
- 

In Algorithm 1, step 1 uses the Tweedie's formula (Chung et al., 2023) to produce a point estimate of the sample  $\hat{\mathbf{x}}_{0,s^*}, \theta$  given a noisy sample  $\mathbf{x}_{t,s^*}$ . It essentially removes the noise from the noisy sample with the noise estimated by the DeNN  $\epsilon_{\theta}$ . Then, step 1 and 1 use the (scaled) gradient over the clean sample  $\hat{\mathbf{x}}_{0,s^*}, \theta$  to approximate  $\nabla_{\mathbf{x}_{t,s^*}} \log p(\mathbf{c}_{2,s^*} | \mathbf{x}_{t,s^*}, \mathbf{c}_{1,s^*})$ . Such a procedure is easy to implement and works well in practice. We will defer detailed derivations to supplementary materials.

It is the practitioner's discretion to choose the instantiation of  $p(\mathbf{c}_{2,s^*} | \mathbf{x}_{0,s^*}, \mathbf{c}_{1,s^*})$  in Algorithm 1. In principle, the

conditional probability model should reflect how the expensive simulation  $\mathbf{c}_{2,s^*}$  is related to the observations  $\mathbf{x}_{0,s^*}$ . We will demonstrate two choices of conditional probability models in the numerical experiments about fumes (16) and thermal processes (22). In section 3.4, we also present some guidelines for designing the conditional model.

Combining Algorithm 1 with the DDIM discretization of (9), a discrete update rule for sampling/inference is,

$$\begin{aligned} \mathbf{x}_{t-1,s^*} &= \frac{1}{\sqrt{\alpha_t}} \left( \mathbf{x}_{t,s^*} \right. && \text{(Term 1)} \\ &- \frac{1 - \alpha_t}{\sqrt{1 - \bar{\alpha}_t} + \sqrt{\alpha_t - \bar{\alpha}_t}} \boldsymbol{\epsilon}_\theta(\mathbf{x}_{t,s^*}, t, \mathbf{x}_{0,1:s_{\text{ct}}}, \mathbf{c}_{1,s^*}) && \text{(Term 2)} \\ &\left. + (1 - \alpha_t) \mathbf{g}(\mathbf{x}_{0,1:s_{\text{ct}}}, \mathbf{c}_{1,s^*}, \mathbf{c}_{2,s^*}, t) \right), && \text{(Term 3)} \end{aligned} \quad (11)$$

for  $t$  from  $T$  to 1. In (11), (Term 1) corresponds to the  $\frac{\beta_t}{2} \mathbf{x}_{t,s^*}$  component in (9), which is essential in the variance-preserving SDE. (Term 2) approximates the score function that drives the sample  $\mathbf{x}_{t,s^*}$  to high-probability regions predicted by the inexpensive physics simulation  $\mathbf{c}_{1,s^*}$ . The coefficients are consistent with those in DDIM. Furthermore, (Term 3) represents the conditioning of the expensive physics simulation  $\mathbf{c}_{2,s^*}$  that furnishes additional guidance to  $\mathbf{x}_{t,s^*}$ . (Term 3) is the major difference between (11) and (8). The collective effects of three forces encourage the sample to enter regions where statistical patterns and physics knowledge are congruent.

By initializing  $\mathbf{x}_{T,s^*}$  from multiple independent samples from the standard normal distribution and iteratively applying (11), one can obtain multiple instances of  $\mathbf{x}_{0,s^*}$ . The sample variances estimated from these instances provide a straightforward characterization for uncertainty quantification.

To summarize, the pseudocodes of the training and sampling algorithms are presented in Algorithm 2 and Algorithm 3.

---

**Algorithm 2** MPDM: Training of the denoising network  $\boldsymbol{\epsilon}_\theta$

- 1: Input training dataset  $\mathcal{D}_{\text{aug}}$ .
  - 2: **for** Epoch  $n = 1, 2, \dots, B$  **do**
  - 3:   Sample  $\boldsymbol{\epsilon} \sim \mathcal{N}(0, \mathbf{I})$ .
  - 4:   Sample  $(\mathbf{x}_{0,s^*}, \mathbf{x}_{0,1:s_{\text{ct}}}, \mathbf{c}_{1,s^*}) \sim \mathcal{D}_{\text{aug}}$ .
  - 5:   Sample  $t \sim \mathcal{U}[0, T]$ .
  - 6:   Calculate the gradient
 
$$\nabla_\theta \left\| \boldsymbol{\epsilon} - \boldsymbol{\epsilon}_\theta(\sqrt{\alpha_t} \mathbf{x}_{0,s^*} + \sqrt{1 - \bar{\alpha}_t} \boldsymbol{\epsilon}, \mathbf{x}_{0,1:s_{\text{ct}}}, \mathbf{c}_{1,s^*}, t) \right\|^2$$
  - 7:   Update  $\theta$  by the gradient.
  - 8: **end for**
  - 9: Return  $\boldsymbol{\epsilon}_\theta$ .
- 

---

**Algorithm 3** MPDM: Sample from  $p(\mathbf{x}_{0,s^*} | \mathbf{x}_{0,1:s_{\text{ct}}}, \mathbf{c}_{1,s^*}, \mathbf{c}_{2,s^*})$

- 1: Input trained denoising network  $\boldsymbol{\epsilon}_\theta$ ,  $\mathbf{g}$ , context state vectors  $\mathbf{x}_{0,1:s_{\text{ct}}}$ , inexpensive physics output  $\mathbf{c}_{1,s^*}$ , (perhaps) expensive physics output  $\mathbf{c}_{2,s^*}$ .
  - 2: Sample  $\mathbf{x}_{T,s^*} \sim \mathcal{N}(0, \mathbf{I})$ .
  - 3: **for** Index  $t = T, T - 1, \dots, 1$  **do**
  - 4:   **if** (Choice 1)  $\mathbf{c}_{2,s^*}$  is not available **then**
  - 5:     Calculate  $\mathbf{x}_{t-1,s^*}$  from (8).
  - 6:   **end if**
  - 7:   **if** (Choice 2)  $\mathbf{c}_{2,s^*}$  is available **then**
  - 8:     Calculate  $\mathbf{x}_{t-1,s^*}$  from (11).
  - 9:   **end if**
  - 10: **end for**
  - 11: Return  $\mathbf{x}_{0,s^*}$ .
- 

### 3.4. Insights for designing the conditional probability

$$p(\mathbf{c}_{2,s^*} | \mathbf{x}_{0,s^*}, \mathbf{c}_{1,s^*})$$

Leveraging domain-specific knowledge is crucial for determining the exact form of the conditional probability model. In literature, numerous successful examples of such models exist (Jacobsen et al., 2023; Song et al., 2021b).

In scenarios where different physics simulations are independent, it is reasonable to simplify the conditional probability as  $p(\mathbf{c}_{2,s^*} | \mathbf{x}_{0,s^*}, \mathbf{c}_{1,s^*}) = p(\mathbf{c}_{2,s^*} | \mathbf{x}_{0,s^*})$ . Our studies demonstrate that this probability can be effectively represented by energy-based models:  $p(\mathbf{c}_{2,s^*} | \mathbf{x}_{0,s^*}) \propto \exp(-\gamma E(\mathbf{c}_{2,s^*}, \mathbf{x}_{0,s^*}))$ , where  $E$  denotes a differentiable energy function and the partition function is neglected as after taking the logarithm, the partition function contributes only a constant term, which becomes zero if we take gradient on  $\mathbf{x}_{0,s^*}$ . This energy function attains lower values for consistent pairs of simulation  $\mathbf{c}_{2,s^*}$  and sample  $\mathbf{x}_{0,s^*}$  and higher values for inconsistent pairs. For instance, if  $\mathbf{c}_{2,s^*}$  is a coarse-grained prediction for  $\mathbf{x}_{0,s^*}$ , one could define  $E$  as  $E(\mathbf{c}_{2,s^*}, \mathbf{x}_{0,s^*}) = \|\mathbf{c}_{2,s^*} - \mathbf{x}_{0,s^*}\|^2$ .  $\gamma$  serves as a temperature parameter that modulates the strength of the conditional probability. This model framework promotes consistency between the sample and the corresponding expensive physics simulation. We will explore two applications of the energy-based approach in Sections 5 and 6.

## 4. Theoretical Analysis

Now, we provide theoretical guarantees for the sampling algorithms in the continuous regime. Remember that the *raison d'être* for Algorithm 3 is to obtain samples from  $p(\mathbf{x}_{0,s^*} | \mathbf{x}_{0,1:s_{\text{ct}}}, \mathbf{c}_{1,s^*})$  and  $p(\mathbf{x}_{0,s^*} | \mathbf{x}_{0,1:s_{\text{ct}}}, \mathbf{c}_{1,s^*}, \mathbf{c}_{2,s^*})$ . A natural performance metric for the sampler is thus the distance between the ground truth and sampling distribution.

In this section, we use  $q_\theta^{\text{ch}1}(\mathbf{x}_{0,s^*})$  to denote the dis-

tribution of samples generated by Algorithm 3 with choice 1, and  $q_\theta^{\text{ch}2}(\mathbf{x}_{0,s^*})$  to denote the sample distributions from Algorithm 3 with choice 2, where we omit the dependence on  $\mathbf{x}_{0,1:s_{\text{ct}}}$ ,  $\mathbf{c}_{1,s^*}$ , and  $\mathbf{c}_{2,s^*}$  for brevity. Then a well-behaving algorithm should satisfy  $q_\theta^{\text{ch}1}(\mathbf{x}_{0,s^*}) \approx p(\mathbf{x}_{0,s^*} | \mathbf{x}_{0,1:s_{\text{ct}}}, \mathbf{c}_{1,s^*})$  and  $q_\theta^{\text{ch}2}(\mathbf{x}_{0,s^*}) \approx p(\mathbf{x}_{0,s^*} | \mathbf{x}_{0,1:s_{\text{ct}}}, \mathbf{c}_{1,s^*}, \mathbf{c}_{2,s^*})$ . Similar to (Kwon et al., 2022), we use the Wasserstein distance to quantify the difference between the sampling and ground truth distributions. The Wasserstein distance (Santambrogio, 2015) between two p.d.f.  $p_1$  and  $p_2$  is denoted as  $W_2(p_1(\mathbf{x}), p_2(\mathbf{x}))$ .

Intuitively, the differences between the two distributions result from two sources. The first is the inaccurate denoising network: if  $\epsilon_\theta(\cdot)$  cannot learn the score function  $\nabla_{\mathbf{x}_{t,s^*}} \log p(\mathbf{x}_{t,s^*} | \mathbf{x}_{0,1:s_{\text{ct}}}, \mathbf{c}_{1,s^*})$  to high precisions, the sampling distribution can be inaccurate. Mathematically, we define the expected  $\ell_2$ -error between the denoising network prediction and the ground truth score as,

$$\begin{aligned} \mathcal{L}_1 = & \frac{1}{2} \int_0^T \mathbb{E}_{\mathbf{x}_{t,s^*}} \left[ \left\| \frac{\epsilon_\theta(\mathbf{x}_{t,s^*}, \mathbf{x}_{0,1:s_{\text{ct}}}, \mathbf{c}_{1,s^*})}{\sqrt{1 - \bar{\alpha}_t}} \right. \right. \\ & \left. \left. + \nabla_{\mathbf{x}_{t,s^*}} \log p(\mathbf{x}_{t,s^*} | \mathbf{x}_{0,1:s_{\text{ct}}}, \mathbf{c}_{1,s^*}) \right\|^2 \right] \beta_t dt. \end{aligned} \quad (12)$$

The second source of error originates from inaccurate  $\mathbf{g}$  functions: if  $\mathbf{g}$  does not accurately represent the gradient of the log conditional probability, the sampling algorithm can also be problematic.

$$\begin{aligned} \mathcal{L}_2 = & \frac{1}{2} \int_0^T \beta_t \mathbb{E}_{\mathbf{x}_{t,s^*}} \left[ \left\| \mathbf{g}(\mathbf{x}_{t,s^*}, \mathbf{x}_{0,1:s_{\text{ct}}}, \mathbf{c}_{1,s^*}, \mathbf{c}_{2,s^*}) \right. \right. \\ & \left. \left. - \nabla_{\mathbf{x}_{t,s^*}} \log p(\mathbf{c}_{2,s^*} | \mathbf{x}_{t,s^*}, \mathbf{x}_{0,1:s_{\text{ct}}}, \mathbf{c}_{1,s^*}) \right\|^2 \right] dt \end{aligned} \quad (13)$$

The following theorem provides an upper bound on the Wasserstein distance between the sampling and the ground truth distribution.

**Theorem 4.1.** *Under regularity conditions, if we use Algorithm 3 with choice 1 to sample  $\mathbf{x}_{0,s^*}$ , in the continuous limit, the sample distribution  $q_\theta^{\text{ch}1}$  satisfies,*

$$\begin{aligned} W_2(p(\mathbf{x}_{0,s^*} | \mathbf{x}_{0,1:s_{\text{ct}}}, \mathbf{c}_{1,s^*}), q_\theta^{\text{ch}1}(\mathbf{x}_{0,s^*})) \\ = O\left(\sqrt{\mathcal{L}_1} + W_2(p(\mathbf{x}_{T,s^*} | \mathbf{x}_{0,1:s_{\text{ct}}}, \mathbf{c}_{1,s^*}), \mathcal{N}(0, \mathbf{I}))\right). \end{aligned} \quad (14)$$

Similarly, if we use Algorithm 3 with choice 2 to sample  $\mathbf{x}_{0,s^*}$ , in the continuous limit, the sampling distribution  $q_\theta^{\text{ch}2}$  would satisfy,

$$\begin{aligned} W_2(p(\mathbf{x}_{0,s^*} | \mathbf{x}_{0,1:s_{\text{ct}}}, \mathbf{c}_{1,s^*}, \mathbf{c}_{2,s^*}), q_\theta^{\text{ch}2}(\mathbf{x}_{0,s^*})) = O\left( \right. \\ \left. + W_2(p(\mathbf{x}_{T,s^*} | \mathbf{x}_{0,1:s_{\text{ct}}}, \mathbf{c}_{1,s^*}, \mathbf{c}_{2,s^*}), \mathcal{N}(0, \mathbf{I})) \right) \\ \left. + O\left(\sqrt{\mathcal{L}_1 + \mathcal{L}_2}\right). \end{aligned} \quad (15)$$

It is worth noting that in practice, the forward diffusion processes are often designed carefully such that  $p(\mathbf{x}_{T,s} | \mathbf{x}_{0,1:s_{\text{ct}}}, \mathbf{c}_{1,s^*})$  and  $p(\mathbf{x}_{T,s} | \mathbf{x}_{0,1:s_{\text{ct}}}, \mathbf{c}_{1,s^*}, \mathbf{c}_{2,s^*})$  are extremely close to standard normal distributions (Ho et al., 2020). As such, their Wasserstein distance is often insignificant, and the right-hand side of (14) and (15) are dominated by  $\sqrt{\mathcal{L}_1}$  and  $\sqrt{\mathcal{L}_1 + \mathcal{L}_2}$ .

There are a few implications from Theorem 4.1. First, (14) indicates that if we use choice 1 from Algorithm 3, the sampling distribution error is determined by the prediction error of the denoising network  $\mathcal{L}_1$ . This is consistent with our intuition that a more accurate denoising network  $\epsilon_\theta$  will lead to higher-quality samples. Second, (15) suggests that the sampling error for choice 2 is related to the estimation error in both denoising network  $\epsilon_\theta$  and the gradient of the log conditional probability model  $\mathbf{g}$ . Accurate  $\epsilon_\theta$  and  $\mathbf{g}$  estimates would bring the distribution  $q_\theta^{\text{ch}2}$  close to the ground truth  $p(\mathbf{x}_{0,s^*} | \mathbf{x}_{0,1:s_{\text{ct}}}, \mathbf{c}_{1,s^*}, \mathbf{c}_{2,s^*})$ .

Inspired by Kwon et al. (2022), the proof of Theorem 4.1 follows from the contraction property of the Wasserstein distance. We relegate the complete proof to the supplementary materials.

## 5. Fluid system

We first investigate the numerical performance of the proposed MPDM on a fluid system. The dynamics of viscous fluids are described by Navier-Stokes equations, which are nonlinear partial differential equations. In practice, Navier-Stokes equations are often solved by computational fluid dynamics (CFD) programs. Numerous CFD programs have been developed in recent decades, and many of them rely on finite difference methods that solve fluid fields on the grids (Anderson & Wendt, 1995). Like many physics simulators, finite difference CFD methods face tradeoffs between grid resolution and simulation fidelity, which renders MPDM a useful tool to integrate the predictions from CFD simulations with different resolutions and leverage the combined knowledge to make predictions.

### 5.1. Experiment setup

In the numerical study, we analyze the movement of 2D fumes driven by buoyancy and gravity, with the goal of predicting buoyancy fields. We use Boussinesq approximation (Spiegel & Veronis, 1960) to analyze the evolution of the fume system. The ground truth data are generated by running multiple simulations of the fumes with existing high-performance CFD simulators (Mohanani et al., 2019b;a) on fine-grained  $128 \times 128$  grids. More specifically, we randomly initialize the buoyancy and vorticity at time  $s = 0$  and run the simulator from  $s = 0$  to  $s = 10$ . We use the buoyancy field at  $s = 0$  time steps as the context vectors,



and predict the target state at  $s^* = 10$ . Results of  $N = 2384$  simulations from different random initializations are accumulated and then randomly separated into 90% training set and 10% test set. We train the DeNN  $\epsilon_\theta$  on the training set. On the test set, we try to predict  $\mathbf{x}_{0,s^*}$  with the information  $\mathbf{x}_{0,1:s_{ct}}$ ,  $\mathbf{c}_{1,s^*}$ , and possible  $\mathbf{c}_{2,s^*}$ . The buoyancy at  $s^* = 10$  for four samples from the test set is plotted in the last column of Fig. 2.

To apply MPDM, inexpensive physics predictions  $\mathbf{c}_{1,s^*}$  and expensive physics predictions  $\mathbf{c}_{2,s^*}$  are needed. We generate these predictions using the same Navier-Stokes-Boussinesq simulator but on coarser grids. More specifically, for each simulation, we run the fluid simulator from the same initialization as the ground truth but with a grid resolution of  $32 \times 32$ . The buoyancy and vorticity fields at  $s^* = 10$  are the inexpensive physics prediction  $\mathbf{c}_{1,s^*}$ . Similarly, we run the fluid simulator with a grid resolution of  $64 \times 64$  and use the buoyancy as  $\mathbf{c}_{2,s^*}$ .

Four samples of  $\mathbf{c}_{1,s^*}$  are plotted in the first column of Fig. 2. One can observe that the inexpensive simulation can capture the low-frequency patterns of the ground truth while details of fume swirls are blurred. This disparity demonstrates the inherent simulation bias.

In this study, we choose the conditional probability model  $\log p(\mathbf{c}_{2,s^*} | \mathbf{x}_{0,s}, \mathbf{c}_{1,s^*})$  as,

$$\log p(\mathbf{c}_{2,s^*} | \mathbf{x}_{0,s}, \mathbf{c}_{1,s^*}) = C + \gamma \left\| \text{AvgPool}^{2 \times 2}(\mathbf{c}_{2,s^*}) - \text{AvgPool}^{4 \times 4}(\mathbf{x}_{0,s^*}) \right\|^2, \quad (16)$$

where  $\text{AvgPool}^{2 \times 2}$  is an average pooling operation (He et al., 2016) for the patch size of 2 by 2. More precisely, it divides the  $64 \times 64$  buoyancy field into  $32 \times 32$  patches of size  $2 \times 2$ , then calculates the average buoyancy in each patch. Similarly,  $\text{AvgPool}^{4 \times 4}$  is a  $4 \times 4$  pooling operation. The model (16) encourages the low-frequency information of the simulated buoyancy and predicted buoyancy to be matched.  $\gamma$  is a coefficient that measures the confidence of the result from the simulated buoyancy. We simply set it to be 0.01 throughout our experiments.  $C$  is a normalization constant that will become zero after differentiation. Additionally, we find removing the coefficient  $1 - \alpha_t$  in (Term 3) of (11) and directly using  $\mathbf{g}$  in the sampling update is more numerically stable. Therefore, we implement this modified version of the sampling update.

## 5.2. Benchmarks and visual results

With access to physics simulations, we can implement MPDM to predict the ground-truth buoyancy. We use a U-Net (Ronneberger et al., 2015) implemented in (Wang, 2024) as the DeNN. The U-Net structure comprises eight 2D convolutional layers connected via skip connections. The diffusion step input  $t$  first undergoes transformations

through a sequence of sinusoidal functions with varying frequencies, followed by a nonlinear network to output temporal embeddings. These embeddings are then integrated into the intermediate layers of the U-Net through multiplication and addition operations. We use Adam to optimize the U-Net in Algorithm 2.

For comparisons, we also implement benchmark algorithms popular in the literature.

- KOH (Kennedy & O’Hagan, 2000): The Bayesian calibration algorithm (KOH) uses a GP to model the residuals between the physics simulation output and the ground truth. We implement KOH to predict the difference between the ground truth buoyancy and the buoyancy from simulation using a batch-independent multi-output GP model provided by GPytorch (Gardner et al., 2018).
- NN (Raissi et al., 2019): We directly train a deep neural network (a U-Net (Ronneberger et al., 2015)) to predict the future states of a system given historical information. The network is trained without inputs of  $\mathbf{c}_{1,s^*}$  and  $\mathbf{c}_{2,s^*}$ .
- Standard diffusion (S-DDIM): We implement the method described in Section 3.1 to sample target state vectors without the information from physics simulations.

The predictions of KOH, NN, the S-DDIM in Section 3.1, MPDM with inexpensive physics described in Section 3.2, and MPDM with expensive physics described in Section 3.3 are plotted in Fig. 2.

From Fig. 2, we can clearly see that S-DDIM predictions exhibit sharp and vivid details on the small-scale swirling structures of the fume. However, locations of large-scale swirl patterns are not accurate. This indicates that the DeNN learns the localized buoyancy patterns effectively but struggles to understand the long-range physical knowledge. The limitation is addressed when we use inexpensive physics prediction  $\mathbf{c}_{1,s^*}$  as an additional input to the denoising network. Conditioned on the inexpensive physics prediction, samples from MPDM align more closely with the ground truth in terms of large-scale structures. The results imply that the physics knowledge is integrated in MPDM, which reaps benefits from the simulation while mitigating its bias. Furthermore, when  $\mathbf{c}_{2,s^*}$  is available and used in choice 2 of Algorithm 3, the fidelity of the buoyancy prediction further improves, indicating that the more refined physics simulations can boost the quality of prediction.

On the contrary, the KOH model does not add meaningful information to the physics simulation, probably because the GP is known to have expressiveness limitations in the high-dimension regime (Wang et al., 2020). As our prediction is a

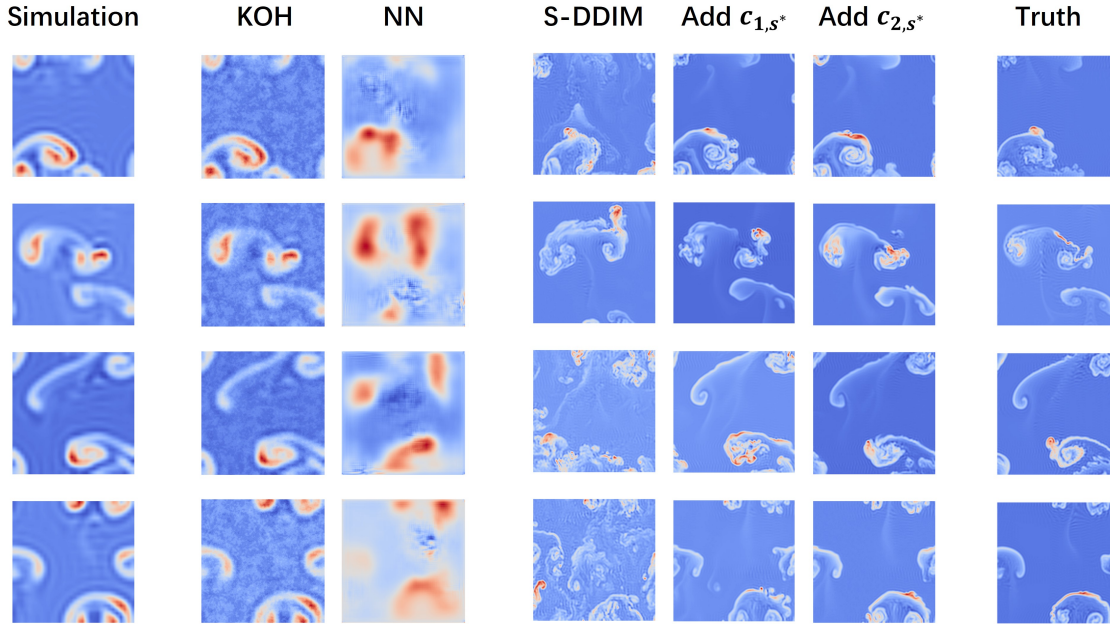


Figure 2. Illustrations of the ground truth buoyancy, physics predictions  $c_{1,s^*}$ , and predictions from 5 different models. 4 random samples are plotted from the test set. Red denotes large buoyancy, and blue denotes low buoyancy. The “Simulation” column contains the output from inexpensive simulations. “S-DDIM” represents the standard diffusion without any physics conditioning. “Add  $c_{1,s^*}$ ” represents the samples from Algorithm 3 with choice 1. “Add  $c_{2,s^*}$ ” represents samples from Algorithm 3 with choice 2.

$128 \times 128 = 16382$  dimensional vector, predicting it using a Gaussian process is uneasy. The NN approach does not give accurate predictions either. This is understandable as NN completely relies on the training set to learn the physical evolution of the fume system. Such a purely statistical approach may not produce decent performance when the training set is not extremely large.

### 5.3. Numerical performance

For numerical comparisons, we also evaluate the quality of the prediction on four standard evaluation metrics: mean squared error (MSE), peak signal-to-noise ratio (PSNR), structural similarity index (SSIM), and learned perceptual image patch similarity (LPIPS) (Zhang et al., 2018). In general, a lower MSE, a higher PSNR, a higher SSIM, and a lower LPIPS indicate a better sample quality. Amongst these metrics, MSE and PSNR measure the low-level pixel-wise difference between the sample and the ground truth, while SSIM is more aligned with human perception of the images. LPIPS leverages a deep neural network (VGG) to capture high-level visual similarities. The mean and standard deviation on the test set are reported in Table 1. In each column, the best result is highlighted in **bold**, while the second-best result is emphasized with an underline.

Results presented in Table 1 corroborate visual observations depicted in Fig. 2. S-DDIM is capable of generating samples that visually resemble the ground truth, as evidenced by its

low LPIPS scores when compared with those from KOH and NN methods. However, the model’s high MSE and low PSNR indicate a poorer alignment with the ground truth at pixel levels.

With inexpensive physics predictions  $c_{1,s^*}$ , MPDM enhances the sample quality as the LPIPS decreases. Furthermore, there are noticeable improvements in MSE, PSNR, and SSIM relative to the standard DDMs. Incorporation of the expensive physics simulation  $c_{2,s^*}$  into the reverse diffusion process (11) leads to even greater improvements. The LPIPS scores decrease further, and the MSE, PSNR, and SSIM reach the highest values compared to all other evaluated algorithms. These improvements substantiate the benefits of utilizing multiple simulations in Algorithm 3.

In comparison, the benchmark KOH and NN incur high LPIPS, corroborating our observations that these samples do not show consistent visual patterns as the ground truth. The comparisons highlight the advantages of the proposed MPDM in producing high-quality results.

## 6. Thermal process in 3D printing

We further apply MPDM on a real-life process of laser-based metal additive manufacturing (LBMAM). LBMAM uses a laser beam to heat and melt metal powders deposited on the printbed to print 3D objects layer by layer (Grasso & Colosimo, 2019; Shi et al., 2024). To monitor the manu-

Table 1. The mean and standard deviation of the sample quality of different algorithms.

	MSE (0.01)↓	PSNR↑	SSIM ↑	LPIPS↓
KOH	<b>1.6</b> (0.1)	<u>19.0</u> (0.3)	<u>99.86</u> (0.01)	0.582(0.004)
NN	<u>1.8</u> (0.1)	18.2(0.2)	99.83(0.01)	0.634(0.006)
S-DDIM	5.6(0.2)	13.2(0.2)	99.48(0.02)	0.555(0.003)
With $c_{1,s^*}$	3.6(0.1)	15.4(0.2)	99.69(0.01)	<u>0.406</u> (0.006)
With $c_{2,s^*}$	<b>1.6</b> (0.1)	<b>19.2</b> (0.3)	<b>99.89</b> (0.01)	<b>0.345</b> (0.006)

facturing process, a thermal camera is installed to capture in-situ temperature distribution on the printing surface. The thermography provides rich information for characterizing the process and potentially identifying defects (Scime & Beuth, 2019; Guo et al., 2023). From a statistics perspective, we aim to predict a future frame of the thermal video, given some observed frames and the information about the movement of the laser that can be recovered from the G-code of the printer.

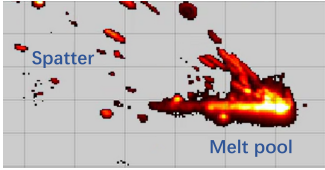


Figure 3. The comet-shaped melt pool and spatters in LBMAM.

A typical thermal frame from an LBMAM process is plotted in Fig. 3, where the underlying physics in the thermal process can roughly be divided into the melt pool’s heat dissipation and the spatters’ movement (Guo et al., 2022; Grasso et al., 2018). We use two ad-hoc physics models to simulate them. The melt pool is the connected high-temperature region around the laser beam. Its dynamics are described by a 2D heat equation, which has a simple closed-form solution in the ideal case. The solution is easy to calculate; hence we model it as  $c_{1,s^*}$ . The spatters are more volatile and irregular. We use a flow model to describe its movement. Compared to the heat pool PDE, the flow model incurs a higher computational cost. Thus, we model the flow velocity field as  $c_{2,s^*}$ . We will describe the details of the two models in this section. It is worth noting that both physics models are oversimplified and thus biased, yet our goal is to fuse data with inaccurate physics simulations to get superior predictions.

For notational consistency, we use  $\mathbf{x}$  to denote the pixelated vectorized frame in a thermal video. If the frame has resolution  $W \times H$ , then  $\mathbf{x}$  is a vector  $\mathbf{x} \in \mathbb{R}^{WH}$ . With a slight abuse of notation, we use  $(x, y)$  to denote the continuous spatial coordinate on the 2D plane. We sometimes use the abbreviated notation  $\mathbf{r} = (x, y)^\top$ . Furthermore, we use  $u(x, y, s)$  to denote a time-varying temperature field on

2D:  $u : \mathbb{R}^2 \times \mathbb{R}^+ \rightarrow \mathbb{R}$ . We use subscripts  $u_m$  and  $u_p$  to represent the temperature field of the melt pool and spatters. A thermal video frame  $\mathbf{x}$  naturally corresponds to the temperature  $u$  at  $W$  by  $H$  grid locations.

## 6.1. Dynamics of the melt pool

The melt pool often displays comet-like shapes, which is a result of heat dissipation and laser movement. In this section, we will construct a computationally amenable model to simulate the morphology and dynamics of the melt pool.

### 6.1.1. HEAT EQUATION

We use  $u_m(x, y, s)$  to denote the melt pool temperature at point  $(x, y)$  at time  $s$ .

A natural way to model the physics of  $u_m$  is the 2D heat equation,

$$\frac{\partial u_m}{\partial s} = \nabla \cdot \kappa \nabla u_m - \rho u_m + f(x, y, s), \quad (17)$$

where the term  $\nabla \cdot \kappa \nabla u_m$  represents heat dissipation.  $\kappa$  is the thermal diffusivity matrix,

$$\kappa = \begin{pmatrix} \kappa_x & 0 \\ 0 & \kappa_y \end{pmatrix}. \quad (18)$$

Term  $-\rho u_m$  represents the loss of heat from the printing surface into the air, and  $f(x, y, s)$  represents the energy injected by the laser beam at  $(x, y, s)$ .

### 6.1.2. SOLUTION IN THE IDEAL CASE

Exactly solving (17) is uneasy as the diffusivity  $\kappa$  can be anisotropic and temperature-dependent and location-dependent, and the same for the parameter  $\rho$ . The boundary condition can also be complicated. Conventional physics simulators are often based on discrete element analysis (Lee & Zhang, 2015) or SPH (Russell et al., 2018).

To obtain a conceptually simple and computationally tractable physical solution, we can make a few simplifying assumptions. We assume  $\kappa$  and  $\rho$  are temperature-independent constants. The initial condition is  $u_m(x, y, 0) = 0$ . And the 2D plane extends to infinity.

Then the solution to (17) is given by,

$$u_m(x, y, s; \phi) = \int_{-\infty}^{\infty} \int_{-\infty}^{\infty} \int_{s'=0}^s G(x, y, s; x', y', s'; \phi) \times f(x', y', s') ds' dx' dy', \quad (19)$$

where  $G(x, y, s; x', y', s'; \phi)$  is the Green's function,

$$G(x, y, s; x', y', s'; \phi) = C_n \exp(-\rho(s - s')) \times \exp\left(-\frac{(\mathbf{r} - \mathbf{r}')^\top \kappa^{-1} (\mathbf{r} - \mathbf{r}')}{4(s - s')}\right), \quad (20)$$

and  $\phi = (\rho, \kappa_x, \kappa_y, C_n)$  denotes the system parameters.

In (19),  $f(x, y, s)$  is given by the Gcode of 3D printers. Therefore, the evolution of temperature  $u_m$  is controlled by only 4 parameters  $\kappa_x$ ,  $\kappa_y$ ,  $\rho$ , and  $C_n$ . We calibrate these four parameters from data using nonlinear least squares. More specifically, on a dataset of observed temperature on grid  $\{u_m^{(i)}\}_{i=1}^N$ , we optimize parameter  $\phi$  to fit the observations by empirical error minimization  $\min_{\phi} \frac{1}{N} \sum_{i=1}^N \left\| u_m^{(i)} - u_m(\cdot; \phi) \right\|^2$ , where  $u_m(\cdot; \phi)$  denotes the temperature  $u_m$  evaluated at grid points. Since the empirical loss is differentiable, the minimization is implemented by Adam. Though  $C_n$  is fixed in theoretical derivation (20), we still calibrate it from data to adapt to the different scalings of  $f$  and  $u_m$ .

With calibrated parameters  $\hat{\phi}$ , we use the value of  $u_m(\cdot; \hat{\phi})$  from equation (19) at  $W$  by  $H$  grid points as  $\mathbf{c}_{1,s^*}$  in Algorithm 3.

## 6.2. Dynamics of the spatters

The interaction between high-energy laser beams and metal powders generates high-temperature particles that scatter from the metal surface. These particles can also be captured by the thermal camera. However, the 2D heat dissipation PDE can hardly describe the movement of particles. As a result, an alternative physics model is needed.

As the high-temperature particles are heated by the energy from the laser, it is natural to model them to be created at the center of the melt pool. After generation, these particles will move toward the edge of the receptive field of the thermal camera. The optical flow model (Horn & Schunck, 1981) provides a suitable characterization for such an emanating movement pattern.

More specifically, we define a velocity field  $\mathbf{v}(x, y, s) = [v_x, v_y]^\top \in \mathbb{R}^2$  denoting the velocity of the particle at position  $(x, y)$  and time  $s$ . The velocity field  $\mathbf{v}$  is the expensive physics simulation  $\mathbf{c}_{2,s}$ . We use  $v_x$  to denote the velocity along the  $x$ -axis and  $v_y$  to denote the velocity at the  $y$ -axis. For a small time interval  $\Delta s$ , the temperature of the scattering particles should remain approximately constant. As a

result,  $u_p$  should satisfy,

$$u_p(x, y, s) = u_p(x - v_x \Delta s, y - v_y \Delta s, s - \Delta s).$$

This equation is widely employed in the literature of optical flows (Horn & Schunck, 1981).

In practice, the optical flow may not be perfectly accurate because of the modeling, measurement, optimization, and statistical errors. We thus use the following probability model to characterize the inaccuracy,

$$u_p(x, y, s) = u_p(x - v_x \Delta s, y - v_y \Delta s, s - \Delta s) + \gamma^{-\frac{1}{2}} \varepsilon, \quad (21)$$

where  $\varepsilon$  are i.i.d. standard Gaussians noise. The parameter  $\gamma$  represents our prior belief about the model accuracy: a larger  $\gamma$  implies a higher confidence in the flow model. Therefore, given the optical flow  $\mathbf{v}$ , the conditional probability is,

$$\log p(\mathbf{v} | u_p(\cdot, \cdot, s), u_p(\cdot, \cdot, s - \Delta s)) = C - \frac{\gamma}{2} \iint (u_p(x, y, s) - u_p(x - v_x \Delta s, y - v_y \Delta s, s - \Delta s))^2 dx dy.$$

Since we predict the temperature only on discrete pixels rather than the continuous 2D plane, the discrete counterpart of the equation above is,

$$\log p(\mathbf{v} | \mathbf{x}_{0,s^*}, \mathbf{x}_{0,s^*-1}) = C + \frac{\gamma}{2} \left\| \mathcal{P}_{\Omega_{\text{spatter}}} (\mathcal{W}(\mathbf{x}_{0,s^*-1}, \mathbf{v}) - \mathbf{x}_{0,s^*}) \right\|^2, \quad (22)$$

where  $\mathbf{v}$  plays the role of the expensive simulation  $\mathbf{c}_{2,s^*}$ .

In (22),  $\mathcal{W}$  denotes the warping operator, which employs a semi-Lagrangian method to infer  $\mathbf{x}_{0,s^*}$  from  $\mathbf{x}_{0,s^*-1}$  and  $\mathbf{v}$ . A more detailed definition of  $\mathcal{W}$  will be provided in the supplementary material.  $\mathcal{P}_{\Omega_{\text{spatter}}}$  denotes the projection into the spatter region,  $\Omega_{\text{spatter}}$ , defined as follows,

$$[\mathcal{P}_{\Omega_{\text{spatter}}}(\mathbf{x})]_j = \begin{cases} [\mathbf{x}]_j, & \text{if } j \text{ is a grid point in } \Omega_{\text{spatter}}, \\ 0, & \text{otherwise.} \end{cases}$$

Intuitively,  $\mathcal{P}_{\Omega_{\text{spatter}}}$  applies a mask that selects the spatter temperature distribution from the entire temperature field. In our implementation, we define  $\Omega_{\text{spatter}}$  as the complement of the melt pool region, which we estimate from the PDE solution (19).

It is important to highlight that both  $\mathcal{W}$  and  $\mathcal{P}_{\Omega_{\text{spatter}}}$  are differentiable. Hence, we can plug in (22) into (10) to calculate  $\mathbf{g}$  using auto-differentiation packages. Subsequently, the gradient  $\mathbf{g}$  is used in Algorithm 3 to guide the sampling process with the information from flow field  $\mathbf{v}$ .

## 6.3. Case study

We use a subset of the 2018 AM Benchmark Test Series from NIST (Heigel et al., 2020) as a testbed of the LBMAM

thermal video prediction model. The dataset is collected in an alloy LBMAM process of a bridge structure manufactured in 624 layers. An infrared camera with a frame rate of 1800 frames per second is installed for in-situ thermography.

We select the thermal videos captured when printing the first 50 layers and slice them into video clips, each of which contains 10 frames. The clips where the laser beam moves outside the camera receptive field are discarded since they are not informative. Each clip is a trajectory of the thermal process of LBMAM. On each clip, we use the beginning 2 frames as the context frames and predict the last 5 frames. We also perform an 80%-20% train-test splitting and present the results on the test set.

As discussed, the solution (19) at  $s^*$  is modeled as inexpensive physics predictions  $c_{1,s^*}$ , which is plotted as the first row of Fig. 4. PDE solutions precisely identify the location of the melt pool. However, compared to the real thermal frames, the PDE solutions are excessively smooth, failing to capture the complex geometries of the melt pool and the spatters.

Conversely, S-DDIM generates more realistic and intricate temperature distributions. As illustrated in the second row of Fig. 4, the irregular contours of the melt pool and the spatial arrangement of spatters bear a closer resemblance to those observed in ground truth data. Nevertheless, the positioning of the melt pool, as predicted by S-DDIM, is inaccurate, indicating deficiencies in the model’s capability to track the dynamics of melt pool movement.

MPDM integrates the strengths of both PDE-based solutions and the diffusion model. Using the available  $c_{1,s^*}$ , we train the DeNN by Algorithm 2, as elaborated in Section 3.2. The results are shown in the third row of Fig. 4. These results vividly illustrate how DDMs can enhance the fine geometric details of the melt pool on top of PDE solutions. Our approach improves the accuracy of predicting the locations of the melt pool while simultaneously preserving the detailed realism of the temperature field.

Though the single-frame prediction of inexpensive physics-informed diffusion demonstrates verisimilitude, the spatter patterns across frames are not consistent in Fig. 4. Therefore, we add flow information to model the evolution of spatters as described in Section 6.2. The estimated flow fields on the test frames are plotted as small black arrows in the fourth row of Fig. 4. Then, we use the flow field  $v$  as the expensive physics simulation  $c_{2,s^*}$  and sample thermal frames with Algorithm 3 with choice 2. Results are plotted in the fifth row of Fig. 4. As highlighted by the red arrows, the flow information makes spatter movement patterns more consistent.

For comparisons, we also implement KOH and NN as benchmarks. Detailed implementation procedures conform to the

specifications described in Section 5.2. The resulting predictions are illustrated in Fig. 5.

In Fig. 5, results from NN and KOH are visually distinct from the ground truth. Specifically, the temperature distributions produced by NN appear over-dispersed. Similarly, the predictions by KOH lack meaningful spatter patterns observed in the ground truth data. When compared to the results depicted in Fig. 4, it is evident that both PINN and KOH yield predictions with geometric patterns that are less consistent with those of the ground truth.

#### 6.4. Numerical evaluation

To thoroughly assess the performance of different approaches, we also calculate the PSNR, SSIM, and LPIPS between the predictions and the ground truth. The detailed settings are similar to Section 5.3. Additionally, to evaluate the cross-frame consistency, we leverage the flow model to evaluate the consistency score between frames. The consistency score is defined as

$$\text{Consistency Score} = \sum_s \frac{\|\mathcal{P}_{\Omega_{\text{spatter}}}(\mathcal{W}(\mathbf{x}_{0,s-1}, \mathbf{v}_s) - \mathbf{x}_{0,s})\|^2}{\|\mathcal{P}_{\Omega_{\text{spatter}}}(\mathbf{x}_{0,s-1})\|},$$

where  $\mathbf{v}_s$  is the flow prediction at time  $s$ . The consistency score measures how well the movement of spatters in samples complies with the flow model. Apparently, a lower consistency score signifies a higher level of cross-frame realism. The mean and standard deviation of different metrics evaluated on the test set are reported in Table 2.

Table 2 shows that the PDE solution  $c_{1,s^*}$  significantly improves the sample quality for the diffusion model, as suggested by increases in PSNR and SSIM and a decrease in LPIPS. Such results are consistent with the visual observations in Fig. 4. Additionally, the use of flow fields  $c_{2,s^*}$  further improves the sample quality and drastically decreases the consistency score, which validates the observation in Fig. 4 that the spatter patterns move more consistently.

For benchmark methods, though KOH attains a high PSNR value, its LPIPS score is high, suggesting that while KOH’s predictions are accurate at a pixel level, they do not align well with human perceptual judgments. This observation is supported by Fig. 5, which shows that the modifications introduced by the KOH model to the PDE solutions are minor and barely perceptible. Therefore, similar to PDE solutions, KOH predictions lack spatters. Such results differ significantly from the ground truths in geometric patterns, thus incurring high LPIPS values. Results for the NN model suggest that its sample quality is not satisfactory either compared to MPDM with choice 2.

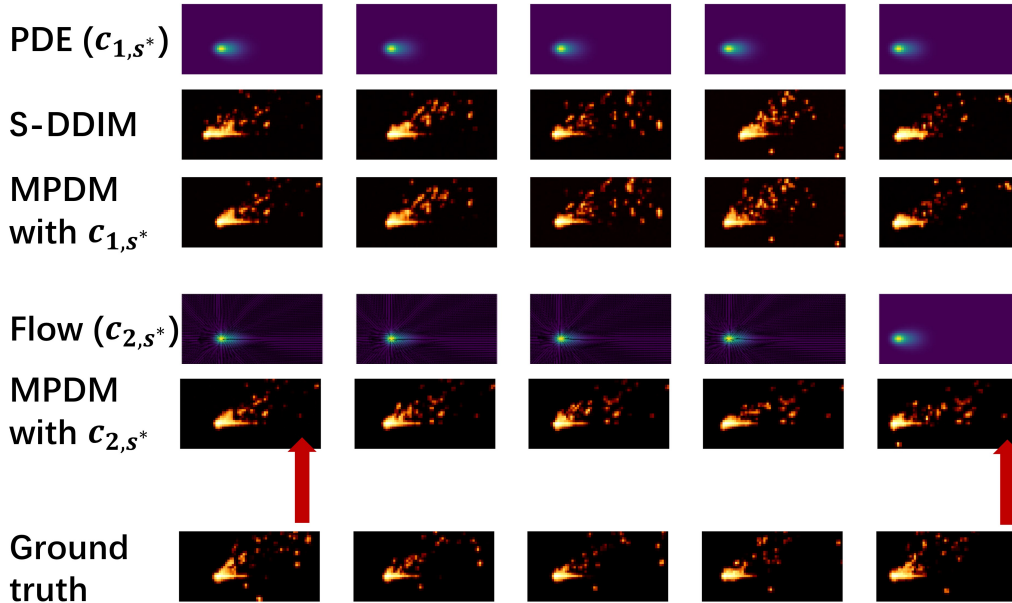


Figure 4. MPDM with guidance from PDE (inexpensive physics) and flow information (expensive physics) on five test frames. White denotes high temperature, and black denotes low temperature.

Table 2. Means and standard deviations of the evaluation metrics for different algorithms. CS denotes the consistency score.

	PSNR $\uparrow$	SSIM $\uparrow$	LPIPS $\downarrow$	CS $\downarrow$
KOH	<b>25.1</b> (0.4)	<u>99.976</u> (0.003)	0.27(0.01)	<u>0.22</u> (0.03)
NN	24.0(0.2)	99.960(0.002)	0.24(0.01)	<b>0.064</b> (0.008)
S-DDIM	21.3(0.2)	99.924(0.004)	0.166(0.002)	1.43(0.03)
With $c_{1,s}^*$	<u>24.3</u> (0.2)	<b>99.977</b> (0.006)	<u>0.140</u> (0.002)	1.41(0.02)
With $c_{2,s}^*$	24.2(0.2)	<u>99.976</u> (0.007)	<b>0.136</b> (0.005)	<b>0.064</b> (0.005)

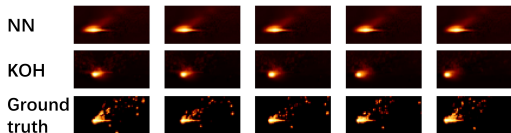


Figure 5. Frame predictions by benchmark methods NN and KOH.

### 6.5. Uncertainty quantification

The probabilistic nature of MPDM provides a straightforward approach to uncertainty quantification. In this case study, we independently sample 40 samples according to standard DDMs and Algorithm 3 with choice 2, and calculate pixel-wise standard deviations of the 40 samples. The results are shown in Fig. 6.

Among benchmark algorithms, only KOH is capable of uncertainty quantification. We thus also plot the standard deviation of the learned GP in KOH in Fig. 6.

Fig. 6 illustrates that the predictive variance of MPDM is

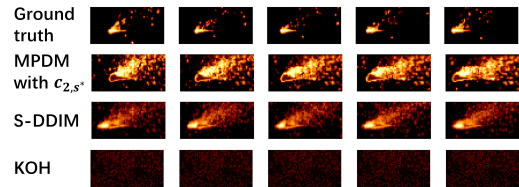


Figure 6. The predictive uncertainty for different methods. S-DDIM stands for standard diffusion without any physics input. White values denote higher levels of uncertainty, and black values denote lower levels of uncertainty.

high in spatter regions and low within the melt pool area. This pattern aligns with expectations, as spatters display irregular and dynamic behaviors in thermal videos, whereas the melt pool movement is more predictable. In contrast, S-DDIM without physics simulation information predicts high variance in the meltpool area, suggesting that the model is unsure about the location of the meltpool. The comparison highlights the advantage of Algorithm (3) in predictive

variance reduction. The predictive uncertainty derived from KOH does not provide meaningful insights. The contrast further illustrates MPDM’s ability to accurately characterize the distribution of the evolution of physical systems.

## 7. Conclusion and future research directions

This paper introduces MPDM, a generative framework based on multi-fidelity physics simulations and diffusion processes. MPDM is proved theoretically well-grounded and exhibits decent performance on the buoyancy and thermal video prediction tasks. We envision that the flexibility of MPDM would engender broader applications in manufacturing and beyond.

In the case studies presented in this paper, the parameters within the physics models are assumed known a priori or are calibrated (by nonlinear least square fitting) prior to deploying the MPDM model. Consequently, an intriguing avenue for future research would be to integrate parameter calibration directly within the probabilistic diffusion model framework. Additionally, the implications of MPDM on experimental design also merit future explorations.

## 8. Supplementary Material

The supplementary material contains the additional derivations in Section 6.1.2 and 6.2 and a formal proof for our main theorem.

## References

- Anderson, J. D. and Wendt, J. *Computational fluid dynamics*, volume 206. Springer, 1995.
- Benjamin, S. G., Brown, J. M., Brunet, G., Lynch, P., Saito, K., and Schlatter, T. W. 100 years of progress in forecasting and nwp applications. *Meteorological Monographs*, 59:13–1, 2019.
- Chen, W., Wu, J., Xie, P., Wu, H., Li, J., Xia, X., Xiao, X., and Lin, L. Control-a-video: Controllable text-to-video generation with diffusion models. *arXiv preprint arXiv:2305.13840*, 2023.
- Chung, H., Kim, J., Mccann, M. T., Klasky, M. L., and Ye, J. C. Diffusion posterior sampling for general noisy inverse problems. In *The Eleventh International Conference on Learning Representations*, 2023. URL <https://openreview.net/forum?id=OnD9zGAGT0k>.
- Chung, H., Lee, S., and Ye, J. C. Decomposed diffusion sampler for accelerating large-scale inverse problems. In *The Twelfth International Conference on Learning Representations*, 2024. URL <https://openreview.net/forum?id=DsEhqQtFAG>.
- Cuomo, S., Di Cola, V. S., Giampaolo, F., Rozza, G., Raissi, M., and Piccialli, F. Scientific machine learning through physics-informed neural networks: Where we are and what’s next. *Journal of Scientific Computing*, 92(3):88, 2022.
- De Bortoli, V., Mathieu, E., Hutchinson, M., Thornton, J., Teh, Y. W., and Doucet, A. Riemannian score-based generative modelling. *Advances in Neural Information Processing Systems*, 35:2406–2422, 2022.
- Fishman, N., Klarner, L., De Bortoli, V., Mathieu, E., and Hutchinson, M. Diffusion models for constrained domains. *arXiv preprint arXiv:2304.05364*, 2023.
- Fonseca Guerra, C., Snijders, J., Te Velde, G. t., and Baerends, E. J. Towards an order-n dft method. *Theoretical Chemistry Accounts*, 99:391–403, 1998.
- Gardner, J., Pleiss, G., Weinberger, K. Q., Bindel, D., and Wilson, A. G. Gpytorch: Blackbox matrix-matrix gaussian process inference with gpu acceleration. *Advances in neural information processing systems*, 31, 2018.
- Gramacy, R. B. *Surrogates: Gaussian process modeling, design, and optimization for the applied sciences*. Chapman and Hall/CRC, 2020.
- Grasso, M. and Colosimo, B. A statistical learning method for image-based monitoring of the plume signature in laser powder bed fusion. *Robotics and Computer-Integrated Manufacturing*, 57:103–115, 2019. ISSN 0736-5845. doi: <https://doi.org/10.1016/j.rcim.2018.11.007>. URL <https://www.sciencedirect.com/science/article/pii/S073658451830139X>.
- Grasso, M., Demir, A., Previtali, B., and Colosimo, B. In situ monitoring of selective laser melting of zinc powder via infrared imaging of the process plume. *Robotics and Computer-Integrated Manufacturing*, 49:229–239, 2018. ISSN 0736-5845. doi: <https://doi.org/10.1016/j.rcim.2017.07.001>. URL <https://www.sciencedirect.com/science/article/pii/S0736584517300583>.
- Guo, S., Agarwal, M., Cooper, C., Tian, Q., Gao, R. X., Guo, W., and Guo, Y. Machine learning for metal additive manufacturing: Towards a physics-informed data-driven paradigm. *Journal of Manufacturing Systems*, 62:145–163, 2022. ISSN 0278-6125. doi: <https://doi.org/10.1016/j.jmsy.2021.11.003>.
- Guo, S., Guo, W., Bian, L., and Guo, Y. B. A deep-learning-based surrogate model for thermal signature prediction in laser metal deposition. *IEEE Transactions on Automation Science and Engineering*, 20(1):482–494, 2023. doi: 10.1109/TASE.2022.3158204.

- He, K., Zhang, X., Ren, S., and Sun, J. Deep residual learning for image recognition. In *Proceedings of the IEEE Conference on Computer Vision and Pattern Recognition (CVPR)*, June 2016.
- Heigel, J. C., Lane, B., Levine, L., Phan, T., and Whiting, J. In situ thermography of the metal bridge structures fabricated for the 2018 additive manufacturing benchmark test series (am-bench 2018). *Journal of Research of the National Institute of Standards and Technology*, 125, 2020.
- Ho, J., Jain, A., and Abbeel, P. Denoising diffusion probabilistic models. *Advances in neural information processing systems*, 33:6840–6851, 2020.
- Ho, J., Chan, W., Saharia, C., Whang, J., Gao, R., Gritsenko, A., Kingma, D. P., Poole, B., Norouzi, M., Fleet, D. J., et al. Imagen video: High definition video generation with diffusion models. *arXiv preprint arXiv:2210.02303*, 2022a.
- Ho, J., Salimans, T., Gritsenko, A., Chan, W., Norouzi, M., and Fleet, D. J. Video diffusion models. *arXiv:2204.03458*, 2022b.
- Horn, B. K. and Schunck, B. G. Determining optical flow. *Artificial intelligence*, 17(1-3):185–203, 1981.
- Huang, C.-W., Aghajohari, M., Bose, J., Panangaden, P., and Courville, A. C. Riemannian diffusion models. *Advances in Neural Information Processing Systems*, 35: 2750–2761, 2022.
- Huang, J., Pang, Y., Liu, Y., and Yan, H. Posterior regularized bayesian neural network incorporating soft and hard knowledge constraints. *Knowledge-Based Systems*, 259: 110043, 2023.
- Iyer, G. Kolmogorov forward equation. *Lecture notes for Advanced Stochastic Calculus*, 2011. URL <https://www.math.cmu.edu/~gautam/teaching/2011-12/880-advanced-scalc/pdfs/kolmogorov-forward.pdf>.
- Jacobsen, C., Zhuang, Y., and Duraisamy, K. Cocogen: Physically-consistent and conditioned score-based generative models for forward and inverse problems. *arXiv preprint arXiv:2312.10527*, 2023.
- Jalal, A., Arvinte, M., Daras, G., Price, E., Dimakis, A. G., and Tamir, J. Robust compressed sensing mri with deep generative priors. *Advances in Neural Information Processing Systems*, 34:14938–14954, 2021.
- Ji, Y., Mak, S., Soeder, D., Paquet, J., and Bass, S. A. A graphical multi-fidelity gaussian process model, with application to emulation of heavy-ion collisions. *Technometrics*, pp. 1–15, 2023.
- Jiao, R., Huang, W., Lin, P., Han, J., Chen, P., Lu, Y., and Liu, Y. Crystal structure prediction by joint equivariant diffusion. *Advances in Neural Information Processing Systems*, 36, 2024.
- Karsch, F. Lattice qed at high temperature and density. In *Lectures on quark matter*, pp. 209–249. Springer, 2002.
- Kennedy, M. C. and O’Hagan, A. Predicting the output from a complex computer code when fast approximations are available. *Biometrika*, 87(1):1–13, 2000.
- Kennedy, M. C. and O’Hagan, A. Bayesian calibration of computer models. *Journal of the Royal Statistical Society: Series B (Statistical Methodology)*, 63(3):425–464, 2001.
- Kollovich, M., Ansari, A. F., Bohlke-Schneider, M., Zschiegner, J., Wang, H., and Wang, Y. B. Predict, refine, synthesize: Self-guiding diffusion models for probabilistic time series forecasting. *Advances in Neural Information Processing Systems*, 36, 2024.
- Kovachki, N., Li, Z., Liu, B., Aizzadenesheli, K., Bhattacharya, K., Stuart, A., and Anandkumar, A. Neural operator: Learning maps between function spaces with applications to pdes. *Journal of Machine Learning Research*, 24(89):1–97, 2023.
- Kwon, D., Fan, Y., and Lee, K. Score-based generative modeling secretly minimizes the wasserstein distance. *Advances in Neural Information Processing Systems*, 35: 20205–20217, 2022.
- Lam, R., Sanchez-Gonzalez, A., Willson, M., Wirnsberger, P., Fortunato, M., Alet, F., Ravuri, S., Ewalds, T., Eaton-Rosen, Z., Hu, W., et al. Learning skillful medium-range global weather forecasting. *Science*, 382(6677):1416–1421, 2023.
- Lee, Y. and Zhang, W. Mesoscopic simulation of heat transfer and fluid flow in laser powder bed additive manufacturing. *2015 International Solid Freeform Fabrication Symposium*, 2015.
- Lewis, P., Perez, E., Piktus, A., Petroni, F., Karpukhin, V., Goyal, N., Küttler, H., Lewis, M., Yih, W.-t., Rocktäschel, T., et al. Retrieval-augmented generation for knowledge-intensive nlp tasks. *Advances in Neural Information Processing Systems*, 33:9459–9474, 2020.
- Li, Y., Lu, X., Wang, Y., and Dou, D. Generative time series forecasting with diffusion, denoise, and disentanglement. In Koyejo, S., Mohamed, S., Agarwal, A., Belgrave, D., Cho, K., and Oh, A. (eds.), *Advances in Neural Information Processing Systems*, volume 35, pp. 23009–23022. Curran Associates, Inc., 2022. URL [https://proceedings.neurips.cc/paper\\_files/paper/2022/file/](https://proceedings.neurips.cc/paper_files/paper/2022/file/)



- 91a85f3fb8f570e6be52b333b5ab017a-Paper-Crombach, R., Blattmann, A., Lorenz, D., Esser, P., and Ommer, B. High-resolution image synthesis with latent diffusion models. In *Proceedings of the IEEE/CVF conference on computer vision and pattern recognition*, pp. 10684–10695, 2022.
- Li, Z., Kovachki, N., Azizzadenesheli, K., Liu, B., Bhattacharya, K., Stuart, A., and Anandkumar, A. Fourier neural operator for parametric partial differential equations. *arXiv preprint arXiv:2010.08895*, 2020.
- Liu, P., Yuan, W., Fu, J., Jiang, Z., Hayashi, H., and Neubig, G. Pre-train, prompt, and predict: A systematic survey of prompting methods in natural language processing. *ACM Computing Surveys*, 55(9):1–35, 2023.
- Lu, L., Jin, P., Pang, G., Zhang, Z., and Karniadakis, G. E. Learning nonlinear operators via deeponet based on the universal approximation theorem of operators. *Nature machine intelligence*, 3(3):218–229, 2021.
- Mak, S., Sung, C.-L., Wang, X., Yeh, S.-T., Chang, Y.-H., Joseph, V. R., Yang, V., and Wu, C. J. An efficient surrogate model for emulation and physics extraction of large eddy simulations. *Journal of the American Statistical Association*, 113(524):1443–1456, 2018.
- Midjourney. Midjourney showcase, 2024. URL <https://www.midjourney.com/showcase>.
- Mohanam, A. V., Bonamy, C., and Augier, P. FluidFFT: Common API (c++ and python) for fast fourier transform HPC libraries. *Journal of Open Research Software*, 7, 2019a. doi: 10.5334/jors.238.
- Mohanam, A. V., Bonamy, C., Linares, M. C., and Augier, P. FluidSim: Modular, Object-Oriented Python Package for High-Performance CFD Simulations. *Journal of Open Research Software*, 7, 2019b. doi: 10.5334/jors.239.
- OpenAI. Video generation models as world simulators, 2024. URL <https://openai.com/research/video-generation-models-as-world-simulators>.
- Raissi, M., Perdikaris, P., and Karniadakis, G. E. Physics informed deep learning (part i): Data-driven solutions of nonlinear partial differential equations. *arXiv preprint arXiv:1711.10561*, 2017.
- Raissi, M., Perdikaris, P., and Karniadakis, G. Physics-informed neural networks: A deep learning framework for solving forward and inverse problems involving nonlinear partial differential equations. *Journal of Computational Physics*, 378:686–707, 2019. ISSN 0021-9991. doi: <https://doi.org/10.1016/j.jcp.2018.10.045>. URL <https://www.sciencedirect.com/science/article/pii/S0021999118307125>.
- Ramesh, A., Dhariwal, P., Nichol, A., Chu, C., and Chen, M. Hierarchical text-conditional image generation with clip latents. *arXiv preprint arXiv:2204.06125*, 1(2):3, 2022.
- Ronneberger, O., Fischer, P., and Brox, T. U-net: Convolutional networks for biomedical image segmentation. In *Medical image computing and computer-assisted intervention—MICCAI 2015: 18th international conference, Munich, Germany, October 5-9, 2015, proceedings, part III 18*, pp. 234–241. Springer, 2015.
- Russell, M., Souto-Iglesias, A., and Zohdi, T. Numerical simulation of laser fusion additive manufacturing processes using the sph method. *Computer Methods in Applied Mechanics and Engineering*, 341:163–187, 2018.
- Santambrogio, F. Optimal transport for applied mathematicians. *Birkäuser, NY*, 55(58-63):94, 2015.
- Scime, L. and Beuth, J. Using machine learning to identify in-situ melt pool signatures indicative of flaw formation in a laser powder bed fusion additive manufacturing process. *Additive Manufacturing*, 25:151–165, 2019. ISSN 2214-8604. doi: <https://doi.org/10.1016/j.addma.2018.11.010>.
- Shi, N., Guo, S., and Al Kontar, R. Personalized feature extraction for manufacturing process signature characterization and anomaly detection. *Journal of Manufacturing Systems*, 74:435–448, 2024.
- Shu, D., Li, Z., and Barati Farimani, A. A physics-informed diffusion model for high-fidelity flow field reconstruction. *Journal of Computational Physics*, 478:111972, 2023. ISSN 0021-9991. doi: <https://doi.org/10.1016/j.jcp.2023.111972>. URL <https://www.sciencedirect.com/science/article/pii/S0021999123000670>.
- Song, J., Meng, C., and Ermon, S. Denoising diffusion implicit models. *arXiv preprint arXiv:2010.02502*, 2020.
- Song, Y. and Ermon, S. Generative modeling by estimating gradients of the data distribution. *Advances in neural information processing systems*, 32, 2019.
- Song, Y., Durkan, C., Murray, I., and Ermon, S. Maximum likelihood training of score-based diffusion models. *Advances in neural information processing systems*, 34: 1415–1428, 2021a.
- Song, Y., Shen, L., Xing, L., and Ermon, S. Solving inverse problems in medical imaging with score-based generative models. *arXiv preprint arXiv:2111.08005*, 2021b.
- Spiegel, E. A. and Veronis, G. On the boussinesq approximation for a compressible fluid. *Astrophysical Journal*, vol. 131, p. 442, 131:442, 1960.

- Spitieris, M. and Steinsland, I. Bayesian calibration of imperfect computer models using physics-informed priors. *Journal of Machine Learning Research*, 24(108):1–39, 2023.
- Stability AI. Stable diffusion 3, 2024. URL <https://stability.ai/stable-image>.
- Sun, L. and Wang, J.-X. Physics-constrained bayesian neural network for fluid flow reconstruction with sparse and noisy data. *Theoretical and Applied Mechanics Letters*, 10(3):161–169, 2020.
- Swiler, L. P., Gulian, M., Frankel, A. L., Safta, C., and Jakeman, J. D. A survey of constrained gaussian process regression: Approaches and implementation challenges. *Journal of Machine Learning for Modeling and Computing*, 1(2), 2020.
- Thieme, H. R. *Mathematics in population biology*, volume 1. Princeton University Press, 2018.
- Urain, J., Funk, N., Peters, J., and Chalvatzaki, G. Se (3)-diffusionfields: Learning smooth cost functions for joint grasp and motion optimization through diffusion. In *2023 IEEE International Conference on Robotics and Automation (ICRA)*, pp. 5923–5930. IEEE, 2023.
- Wang, P. denoising-diffusion-pytorch. <https://github.com/lucidrains/denoising-diffusion-pytorch/tree/main>, 2024.
- Wang, W., Tuo, R., and Jeff Wu, C. On prediction properties of kriging: Uniform error bounds and robustness. *Journal of the American Statistical Association*, 115(530):920–930, 2020.
- Wang, X., Yuan, H., Zhang, S., Chen, D., Wang, J., Zhang, Y., Shen, Y., Zhao, D., and Zhou, J. Videocomposer: Compositional video synthesis with motion controllability. *Advances in Neural Information Processing Systems*, 36, 2024.
- Williams, C. K. and Rasmussen, C. E. *Gaussian processes for machine learning*, volume 2. MIT press Cambridge, MA, 2006.
- Yang, L., Zhang, Z., Song, Y., Hong, S., Xu, R., Zhao, Y., Zhang, W., Cui, B., and Yang, M.-H. Diffusion models: A comprehensive survey of methods and applications. *ACM Computing Surveys*, 56(4):1–39, 2023.
- Yang, W., Lorch, L., Graule, M., Lakkaraju, H., and Doshi-Velez, F. Incorporating interpretable output constraints in bayesian neural networks. *Advances in Neural Information Processing Systems*, 33:12721–12731, 2020.
- Zhang, R., Isola, P., Efros, A. A., Shechtman, E., and Wang, O. The unreasonable effectiveness of deep features as a perceptual metric. In *Proceedings of the IEEE conference on computer vision and pattern recognition*, pp. 586–595, 2018.
- Zhang, R., Liu, Y., and Sun, H. Physics-guided convolutional neural network (phycnn) for data-driven seismic response modeling. *Engineering Structures*, 215:110704, 2020.
- Zhu, Y., Zabararas, N., Koutsourelakis, P.-S., and Perdikaris, P. Physics-constrained deep learning for high-dimensional surrogate modeling and uncertainty quantification without labeled data. *Journal of Computational Physics*, 394: 56–81, 2019.

## A. Derivations in Algorithm 1

In this section, we will discuss the intuitions for Algorithm 1 in the main paper. The goal is to derive an estimate for  $\nabla \log p(\mathbf{c}_{2,s^*} | \mathbf{x}_{t,s^*}, \mathbf{c}_{1,s^*})$ . The derivation is inspired by Chung et al. (2023).

We first use the Bayes law to rewrite  $\log p(\mathbf{c}_{2,s^*} | \mathbf{x}_{t,s^*}, \mathbf{c}_{1,s^*})$  as,

$$\log p(\mathbf{c}_{2,s^*} | \mathbf{x}_{t,s^*}, \mathbf{c}_{1,s^*}) = \log p(\mathbf{x}_{t,s^*} | \mathbf{c}_{1,s^*}) + \log \int p(\mathbf{c}_{2,s^*} | \mathbf{x}_{0,s^*}, \mathbf{x}_{t,s^*}, \mathbf{c}_{1,s^*}) p(\mathbf{x}_{0,s^*} | \mathbf{x}_{t,s^*}, \mathbf{c}_{1,s^*}) d\mathbf{x}_{0,s^*} + C,$$

where  $C$  is a constant independent of  $\mathbf{x}_{0,s^*}$ .

As the integral can be difficult to calculate analytically, we resort to approximations. There are a few feasible approximations, among which we will use the most conceptually simple and computationally tractable one. Since we have trained a denoising network  $\epsilon_\theta(\cdot)$ , we can approximate  $p(\mathbf{x}_{0,s^*} | \mathbf{x}_{t,s^*}, \mathbf{c}_{1,s^*})$  by Tweedie's formula (Chung et al., 2023),

$$p(\mathbf{x}_{0,s^*} | \mathbf{x}_{t,s^*}, \mathbf{c}_{1,s^*}) \approx \delta(\mathbf{x}_{0,s^*} - \hat{\mathbf{x}}_{0,s^*,\theta}(\mathbf{x}_{t,s^*}, \mathbf{c}_{1,s^*}, t)),$$

where  $\delta(\cdot)$  is the Dirichlet-delta function and  $\hat{\mathbf{x}}_{0,s^*,\theta}(\mathbf{x}_{t,s^*}, \mathbf{c}_{1,s^*}, t)$  is defined as,

$$\hat{\mathbf{x}}_{0,s^*,\theta}(\mathbf{x}_{t,s^*}, \mathbf{c}_{1,s^*}, t) = \frac{\mathbf{x}_{t,s^*} - \sqrt{1 - \bar{\alpha}_t} \epsilon_\theta(\mathbf{x}_{t,s^*}, \mathbf{c}_{1,s^*}, t)}{\sqrt{\bar{\alpha}_t}}. \quad (23)$$

With the approximation, we can calculate the gradient as,

$$\nabla_{\mathbf{x}_{t,s}} \log p(\mathbf{c}_{2,s^*} | \mathbf{x}_{t,s^*}, \mathbf{c}_{1,s^*}) \approx \nabla_{\mathbf{x}_{t,s^*}} \log p(\mathbf{c}_{2,s^*} | \hat{\mathbf{x}}_{0,s^*,\theta}(\mathbf{x}_{t,s^*}, \mathbf{c}_{1,s^*}, t), \mathbf{x}_{t,s^*}, \mathbf{c}_{1,s^*}).$$

We can use the Leibniz rule to further expand the gradient as,

$$\nabla_{\mathbf{x}_{t,s^*}} \log p(\mathbf{c}_{2,s^*} | \mathbf{x}_{t,s^*}, \mathbf{x}_{t,s^*}, \mathbf{c}_{1,s^*}) \approx \nabla_{\hat{\mathbf{x}}_{0,s^*,\theta}} \log p(\mathbf{c}_{2,s^*} | \hat{\mathbf{x}}_{0,s^*,\theta}(\mathbf{x}_{t,s^*}, \mathbf{c}_{1,s^*}, t), \mathbf{x}_{t,s^*}, \mathbf{c}_{1,s^*}) \frac{\partial \hat{\mathbf{x}}_{0,s^*,\theta}}{\partial \mathbf{x}_{t,s^*}}.$$

The exact calculation of  $\frac{\partial \hat{\mathbf{x}}_{0,s^*,\theta}}{\partial \mathbf{x}_{t,s^*}}$  requires taking the gradient of a high dimensional variable through a neural network, which can be memory-consuming. To save memory, we thus employ another approximation by ignoring the gradient contributed by the denoising network,  $\frac{\partial \hat{\mathbf{x}}_{0,s^*,\theta}}{\partial \mathbf{x}_{t,s^*}} \approx \frac{1}{\sqrt{\bar{\alpha}_t}} \mathbf{I}$ . Combing these two approximations, we have,

$$\nabla_{\mathbf{x}_{t,s^*}} \log p(\mathbf{c}_{2,s^*} | \mathbf{x}_{t,s^*}(\mathbf{x}_{t,s^*}, \mathbf{c}_{1,s^*}, t), \mathbf{x}_{t,s^*}, \mathbf{c}_{1,s^*}) \approx \frac{1}{\sqrt{\bar{\alpha}_t}} \nabla_{\hat{\mathbf{x}}_{0,s^*,\theta}} \log p(\mathbf{c}_{2,s^*} | \hat{\mathbf{x}}_{0,s^*,\theta}, \mathbf{x}_{t,s^*}, \mathbf{c}_{1,s^*}).$$

## B. Derivations of the solution to the heat equation

The Green's function solves the following equation

$$\frac{\partial}{\partial \tau} G = \nabla \cdot (\kappa \nabla G) - \rho G + \delta(s - s') \delta(\mathbf{r} - \mathbf{r}'), \quad (24)$$

where  $\delta(\cdot)$  is the Dirichlet delta function.

We can use the Fourier transform to solve the equation. Due to translational invariance, the Fourier series of  $G$  is given by,

$$G(\mathbf{r}, s; \mathbf{r}', s') = \int \exp(i\mathbf{k}^\top (\mathbf{r} - \mathbf{r}')) \tilde{G}(\mathbf{k}, s, s') d\mathbf{k}. \quad (25)$$

Therefore, equation (24) becomes,

$$\frac{\partial}{\partial \tau} \tilde{G} = -(\mathbf{k}^\top \kappa \mathbf{k} + \rho) \tilde{G} + \delta(s - s') \exp(-\mathbf{k}^\top (\mathbf{r} - \mathbf{r}')), \quad (26)$$

where we have used the fact  $\delta(\mathbf{r} - \mathbf{r}') = \int \exp(\mathbf{k}^\top(\mathbf{r} - \mathbf{r}')) d\mathbf{k}$ .

When  $s > s'$ , the solution to (26) is simply,

$$\tilde{G}(\mathbf{k}, s, s') = \exp(-\rho(s - s')) \times \exp(-i\mathbf{k}^\top(\mathbf{r} - \mathbf{r}') - \mathbf{k}^\top \kappa \mathbf{k}(s - s')).$$

Therefore, the original Green's function is

$$G(\mathbf{r}, s; \mathbf{r}', s') = \exp(-\rho(s - s')) \left(\frac{1}{\sqrt{2\pi}}\right)^{-1} \left(\frac{\det(\kappa^{-1})}{2(s - s')}\right)^{-1} \exp\left(-\frac{(\mathbf{r} - \mathbf{r}')\kappa^{-1}(\mathbf{r} - \mathbf{r}')}{4(s - s')}\right).$$

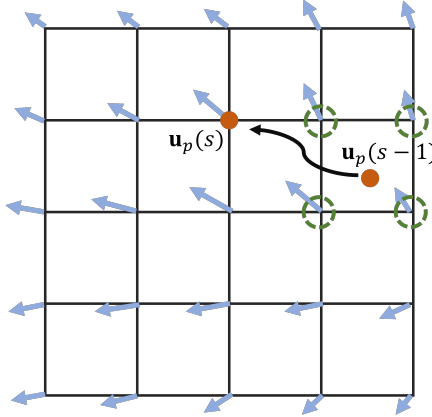
It consists of an exponential decaying component  $\exp(-\rho(s - s'))$ , a Gaussian component  $\exp\left(-\frac{(\mathbf{r} - \mathbf{r}')\kappa^{-1}(\mathbf{r} - \mathbf{r}')}{4(s - s')}\right)$ , and a constant  $C_n = \left(\frac{1}{\sqrt{2\pi}}\right)^{-1} \left(\frac{\det(\kappa^{-1})}{2(s - s')}\right)^{-1}$ .

### C. Optical flow and wrapping

As discussed,  $\mathbf{x}_{0,s-1}$  represents the vectorized temperature at time  $s - 1$  evaluated on the  $W \times H$  grids. We also use  $\mathbf{v}$  to denote the velocity on the same grids. The wrapping operator uses  $\mathbf{v}$  and  $\mathbf{x}_{0,s-1}$  to predict  $\mathbf{x}_{0,s}$ , which is the temperature at time  $s$  defined on the  $W \times H$  grids.

We implement the wrapping operator via a semi-Lagrangian approach. An illustration of the numerical advection is shown in Fig. 7.

Figure 7. An illustration of the advection and the wrapping operator. Blue arrows denote velocity defined on grids. The orange dot is traced back in time.



More specifically, for any grid location  $(x, y)$ , the algorithm estimates its location at time  $s - 1$  as  $(x - v_x, y - v_y)$ , then predict  $u(x, y, t)$  as  $u(x - v_x, y - v_y, s - 1)$ . However, as shown in Fig. 7, the orange dot representing  $(x - v_x, y - v_y)$  may not sit exactly on the grid point. Thus,  $u(x - v_x, y - v_y, s - 1)$  is not readily known. To resolve the issue, we use bilinear interpolation to interpolate the velocity  $u(x - v_x, y - v_y, s - 1)$  based on the grid velocity  $\mathbf{x}_{0,s-1}$  on the closest grids, which are shown as the green circles in Fig. 7.

We provide a pseudo-code for the wrapping operator as,

In Algorithm 4, `interpolate` is the standard bilinear interpolation from the closest grid points. The entire operation is differentiable.

### D. Proof for Theorem 4.1

In this section, we present the proof for Theorem 4.1 in the main paper. In literature, the Wasserstein distance is defined as,

$$W_2(p_1(\mathbf{x}), p_2(\mathbf{x})) = \min_{\pi \in \Pi(p_1, p_2)} \left( \int \|\mathbf{x} - \mathbf{y}\|^2 d\pi(\mathbf{x}, \mathbf{y}) \right)^{\frac{1}{2}}, \quad (27)$$

**Algorithm 4** The wrapping operator  $\mathcal{W}$

---

- 1: Input  $\mathbf{x}_{0,s-1}, v_x, v_y$  defined on  $W \times H$  grids.
  - 2: **for** Row index  $i = 1, \dots, H$  **do**
  - 3:   **for** Column index  $j = 1, \dots, W$  **do**
  - 4:     Calculate  $(j - v_y(i, j), i - v_x(i, j))$ .
  - 5:     Calculate  $u(i, j, s) = \text{interpolate}(\mathbf{x}_{0,s-1}, j - v_y, i - v_x)$ .
  - 6:   **end for**
  - 7: **end for**
  - 8: Calculate  $\mathbf{x}_{0,s}^{\text{pred}}$  by stacking values of  $u(i, j, s)$ .
  - 9: Return  $\mathbf{x}_{0,s}^{\text{pred}}$ .
- 

where  $\Pi(p_1, p_2)$  is the set of all joint distributions of  $(\mathbf{x}, \mathbf{y})$  whose marginal distributions are  $p_1(\mathbf{x})$  and  $p_2(\mathbf{y})$ .

We will begin by introducing a useful inequality that provides an upper bound of the Wasserstein distance between the distributions given by two PDEs. Similar versions of this inequality have already been derived in literature (Kwon et al., 2022).

**Lemma D.1.** Consider two p.d.f.  $p_{1,t}(\mathbf{x})$  and  $p_{2,t}(\mathbf{x})$  in  $\mathbb{R}^d$  that satisfy the following PDEs respectively,

$$\frac{\partial}{\partial t} p_{1,t}(\mathbf{x}) + \nabla \cdot (p_{1,t}(\mathbf{x}) \mu_1(\mathbf{x}, t)) = 0, \quad (\text{PDE1})$$

$$\frac{\partial}{\partial t} p_{2,t}(\mathbf{x}) + \nabla \cdot (p_{2,t}(\mathbf{x}) \mu_2(\mathbf{x}, t)) = 0. \quad (\text{PDE2})$$

where  $\mu_1, \mu_2 \in \mathbb{R}^d$  are drift terms that satisfy the regularity conditions in (Kwon et al., 2022). If additionally, there exists a finite function  $L_1(t)$ , such that for each  $t \in [0, T]$ ,  $|(\mathbf{x} - \mathbf{y})^\top (\mu_2(\mathbf{x}, t) - \mu_2(\mathbf{y}, t))| \leq L_1(t) \|\mathbf{x} - \mathbf{y}\|^2, \forall \mathbf{x}, \mathbf{y} \in \mathbb{R}^d$ , then, the Wasserstein distance satisfies

$$W_2(p_{1,0}, p_{2,0}) \leq W_2(p_{1,T}, p_{2,T}) \exp\left(\int_0^T L_1(r) dr\right) + \int_0^T \exp\left(\int_0^r L_1(r) dt\right) \mathbb{E}_{\mathbf{x} \sim p_{1,t}(\mathbf{x})} \left[ \|\mu_1(\mathbf{x}, t) - \mu_2(\mathbf{x}, t)\|^2 \right]^{\frac{1}{2}} dt.$$

We outline the proof of Lemma D.1 for completeness.

*Proof.* The proof follows (Kwon et al., 2022).

Corollary 5.25 in (Santambrogio, 2015) provides an important relation that describes the evolution of the Wasserstein distance between  $p_{1,t}$  and  $p_{2,t}$ ,

$$\frac{1}{2} \frac{d}{dt} W_2^2(p_{1,t}, p_{2,t}) = \mathbb{E}_{(\mathbf{x}, \mathbf{y}) \sim \pi_t} \left[ (\mathbf{x} - \mathbf{y})^\top (\mu_1(\mathbf{x}, t) - \mu_2(\mathbf{y}, t)) \right] \quad (28)$$

under regularity conditions, where  $\pi_t$  is the optimal transport map from  $p_{1,t}$  to  $p_{2,t}$ .

The right hand side of (28) can be expanded as,

$$(\mathbf{x} - \mathbf{y})^\top (\mu_1(\mathbf{x}, t) - \mu_2(\mathbf{y}, t)) = (\mathbf{x} - \mathbf{y})^\top (\mu_1(\mathbf{x}, t) - \mu_2(\mathbf{x}, t)) + (\mathbf{x} - \mathbf{y})^\top (\mu_2(\mathbf{x}, t) - \mu_2(\mathbf{y}, t))$$

For the first term, Cauchy-Schwartz inequality indicates,

$$\begin{aligned} & \mathbb{E}_{(\mathbf{x}, \mathbf{y}) \sim \pi_t} \left[ (\mathbf{x} - \mathbf{y})^\top (\mu_1(\mathbf{x}, t) - \mu_2(\mathbf{x}, t)) \right] \\ & \geq -\mathbb{E}_{(\mathbf{x}, \mathbf{y}) \sim \pi_t} \left[ \|\mathbf{x} - \mathbf{y}\|^2 \right]^{\frac{1}{2}} \mathbb{E}_{(\mathbf{x}, \mathbf{y}) \sim \pi_t} \left[ \|\mu_1(\mathbf{x}, t) - \mu_2(\mathbf{x}, t)\|^2 \right]^{\frac{1}{2}} \\ & = W_2(p_{1,t}, p_{2,t}) \mathbb{E}_{\mathbf{x} \sim p_{1,t}} \left[ \|\mu_1(\mathbf{x}, t) - \mu_2(\mathbf{x}, t)\|^2 \right]^{\frac{1}{2}} \end{aligned}$$

The second term can be lower bounded by the assumption of Lipschitz continuity,

$$\begin{aligned} & \mathbb{E}_{(\mathbf{x}, \mathbf{y}) \sim \pi_t} \left[ (\mathbf{x} - \mathbf{y})^\top (\mu_2(\mathbf{x}, t) - \mu_2(\mathbf{y}, t)) \right] \\ & \geq -\mathbb{E}_{(\mathbf{x}, \mathbf{y}) \sim \pi_t} \left[ L_2(t) \|\mathbf{x} - \mathbf{y}\|^2 \right] = -L_2(t) W_2^2(p_{1,t}, p_{2,t}) \end{aligned}$$

Combining them, we know that

$$\frac{1}{2} \frac{d}{dt} W_2(p_{1,t}, p_{2,t}) \geq -W_2^2(p_{1,t}, p_{2,t}) \mathbb{E}_{\mathbf{x} \sim p_{1,t}} \left[ \|\mu_1(\mathbf{x}, t) - \mu_2(\mathbf{x}, t)\|^2 \right]^{\frac{1}{2}} - L_2(t) W_2^2(p_{1,t}, p_{2,t}).$$

This implies,

$$\frac{d}{dt} \left( \exp \left( \int_0^t L_1(r) dr \right) W_2(p_{1,t}, p_{2,t}) \right) \geq -\exp \left( \int_0^t L_1(r) dr \right) \mathbb{E}_{\mathbf{x} \sim p_{1,t}} \left[ \|\mu_1(\mathbf{x}, t) - \mu_2(\mathbf{x}, t)\|^2 \right]^{\frac{1}{2}}. \quad (29)$$

By integrating both sides for  $t$  from 1 to  $T$ , we complete the proof.  $\square$

With Lemma D.1, we can prove Theorem 4.1 in the main paper. We assume the regularity conditions in (Kwon et al., 2022) are satisfied. Additionally, we assume that there are constants  $L_\epsilon, L_g > 0$ , such that for all possible tuple  $(\mathbf{x}_{0,1:s_{ct}}, \mathbf{c}_{1,s^*}, \mathbf{c}_{2,s^*}, t)$ , the following holds,

$$\begin{cases} \left| (\mathbf{x} - \mathbf{y})^\top (\epsilon_\theta(\mathbf{x}, \mathbf{x}_{0,1:s_{ct}}, \mathbf{c}_{1,s^*}) - \epsilon_\theta(\mathbf{y}, \mathbf{x}_{0,1:s_{ct}}, \mathbf{c}_{1,s^*})) \right| \leq L_\epsilon \|\mathbf{x} - \mathbf{y}\|^2 \\ \left| (\mathbf{x} - \mathbf{y})^\top (g(\mathbf{x}, \mathbf{c}_{1,s^*}, \mathbf{c}_{2,s^*}) - g(\mathbf{y}, \mathbf{c}_{1,s^*}, \mathbf{c}_{2,s^*})) \right| \leq L_g \|\mathbf{x} - \mathbf{y}\|^2 \end{cases} \quad \forall \mathbf{x}, \mathbf{y} \in \mathbb{R}^d \quad (30)$$

*Proof.* We first consider the sampling algorithm with choice 1. In the continuous regime, the forward diffusion process is characterized by

$$d\mathbf{x}_{t,s^*} = -\frac{\beta_t}{2} \mathbf{x}_{t,s^*} dt + \sqrt{\beta_t} d\mathbf{w}_t.$$

The forward Kolmogorov equation (Iyer, 2011) shows that the p.d.f.  $p(\mathbf{x}_{t,s^*} | \mathbf{x}_{0,1:s_{ct}}, \mathbf{c}_{1,s^*})$  follows a PDE,

$$\frac{\partial}{\partial t} p(\mathbf{x}_{t,s^*} | \mathbf{x}_{0,1:s_{ct}}, \mathbf{c}_{1,s^*}) + \nabla \cdot \left( p(\mathbf{x}_{t,s^*} | \mathbf{x}_{0,1:s_{ct}}, \mathbf{c}_{1,s^*}) \left( -\frac{\beta_t}{2} \mathbf{x} - \frac{\beta_t}{2} \nabla \log p(\mathbf{x}_{t,s^*} | \mathbf{x}_{0,1:s_{ct}}, \mathbf{c}_{1,s^*}) \right) \right) = 0$$

As discussed, the sampling algorithm with choice 1 reduces to an ODE in the continuous regime,

$$d\mathbf{x}_{t,s^*} = \left( \frac{\beta_t}{2} \mathbf{x}_{t,s^*} - \frac{\beta_t}{2\sqrt{1-\bar{\alpha}_t}} \epsilon_\theta(\mathbf{x}_{t,s^*}, \mathbf{x}_{0,1:s_{ct}}, \mathbf{c}_{1,s^*}) \right) \quad (31)$$

and initializes  $\mathbf{x}_{T,s}$  from the standard normal distribution  $\mathcal{N}(0, \mathbf{I})$ . By forward Kolmogorov equation, the p.d.f. of  $\mathbf{x}_{s,t}, q_\theta^{\text{ch } 1}$ , satisfy,

$$\frac{\partial}{\partial t} q_\theta^{\text{ch } 1}(\mathbf{x}_{t,s^*}) + \nabla \cdot \left( q_\theta^{\text{ch } 1}(\mathbf{x}_{t,s^*}) \left( -\frac{\beta_t}{2} \mathbf{x}_{t,s^*} + \frac{\beta_t}{2} \frac{\epsilon_\theta(\mathbf{x}_{t,s^*}, \mathbf{x}_{0,1:s_{ct}}, \mathbf{c}_{1,s^*})}{\sqrt{1-\bar{\alpha}_t}} \right) \right) = 0$$

It is straightforward to set  $\mu_1(\mathbf{x}_{t,s^*}) = -\frac{\beta_t}{2} \mathbf{x}_{t,s^*} + \frac{\beta_t}{2} \nabla \log p(\mathbf{x}_{t,s^*} | \mathbf{x}_{0,1:s_{ct}}, \mathbf{c}_{1,s^*})$ ,  $\mu_2(\mathbf{x}_{t,s^*}) = -\frac{\beta_t}{2} \mathbf{x}_{t,s^*} - \frac{\beta_t}{2\sqrt{1-\bar{\alpha}_t}} \epsilon_\theta(\mathbf{x}_{t,s^*}, \mathbf{x}_{0,1:s_{ct}}, \mathbf{c}_{1,s^*})$ , and apply Lemma D.1. We first provide an upper bound of the Lipschitz constant  $L_1$  from the assumptions. For any  $\mathbf{x}, \mathbf{y} \in \mathbb{R}^d$ , we have,

$$\begin{aligned} & |(\mathbf{x} - \mathbf{y})^\top (\mu_2(\mathbf{x}, t) - \mu_2(\mathbf{y}, t))| \\ & = \left| (\mathbf{x} - \mathbf{y})^\top \left( \frac{\beta_t}{2} (\mathbf{x} - \mathbf{y}) + \frac{\beta_t}{2\sqrt{1-\bar{\alpha}_t}} (\epsilon_\theta(\mathbf{x}) - \epsilon_\theta(\mathbf{y})) \right) \right| \\ & \leq \frac{\beta_t}{2} \|\mathbf{x} - \mathbf{y}\|^2 + \frac{\beta_t}{2\sqrt{1-\bar{\alpha}_t}} |(\mathbf{x} - \mathbf{y})^\top (\epsilon_\theta(\mathbf{x}) - \epsilon_\theta(\mathbf{y}))| \\ & \leq \frac{1+L_\epsilon}{2} \|\mathbf{x} - \mathbf{y}\|^2, \end{aligned}$$

where we used the inequality  $\frac{\beta_t}{2\sqrt{1-\bar{\alpha}_t}} \leq \frac{\beta_t}{2\sqrt{\beta_t}}$  and  $\beta_t < 1$ .

Therefore, Lemma D.1 implies,

$$\begin{aligned} & \mathbf{W}_2 \left( p(\mathbf{x}_{0,s^*} | \mathbf{x}_{0,1:s_{\text{ct}}}, \mathbf{c}_{1,s^*}), q_{\theta}^{\text{ch}1}(\mathbf{x}_{0,s^*}) \right) \\ & \leq \mathbf{W}_2 \left( p(\mathbf{x}_{T,s^*} | \mathbf{x}_{0,1:s_{\text{ct}}}, \mathbf{c}_{1,s^*}), \mathcal{N}(0, \mathbf{I}) \right) \exp \left( T \frac{1+L_{\epsilon}}{2} \right) \\ & \quad + \int_0^T \exp \left( t \frac{1+L_{\epsilon}}{2} \right) \frac{\beta_t}{2} \mathbb{E}_{p_t(\mathbf{x}_{t,s^*})} \left[ \left\| \nabla p(\mathbf{x}_{t,s^*} | \mathbf{x}_{0,1:s_{\text{ct}}}, \mathbf{c}_{1,s^*}) + \frac{\boldsymbol{\epsilon}_{\theta}(\mathbf{x}_{t,s^*}, \mathbf{x}_{0,1:s_{\text{ct}}}, \mathbf{c}_{1,s^*})}{\sqrt{1-\bar{\alpha}}} \right\|^2 \right]^{\frac{1}{2}} dt \\ & \leq \mathbf{W}_2 \left( p(\mathbf{x}_{T,s^*} | \mathbf{x}_{0,1:s_{\text{ct}}}, \mathbf{c}_{1,s^*}), q_{\theta}^{\text{ch}1}(\mathbf{x}_{T,s^*}) \right) \exp \left( T \frac{1+L_{\epsilon}}{2} \right) + \left( \int_0^T \exp(t(1+L_{\epsilon})) \frac{\beta_t}{2} dt \right)^{\frac{1}{2}} \times \sqrt{\mathcal{L}_1} \end{aligned}$$

where we used Cauchy-Schwartz inequality in the last inequality and  $\mathcal{L}_1$  is defined as,

$$\mathcal{L}_1 = \frac{1}{2} \int_0^T \beta_t \mathbb{E}_{p_t(\mathbf{x}_{t,s^*})} \left[ \left\| \nabla p(\mathbf{x}_{t,s^*} | \mathbf{x}_{0,1:s_{\text{ct}}}, \mathbf{c}_{1,s^*}) + \frac{\boldsymbol{\epsilon}_{\theta}(\mathbf{x}_{t,s^*}, \mathbf{x}_{0,1:s_{\text{ct}}}, \mathbf{c}_{1,s^*})}{\sqrt{1-\bar{\alpha}}} \right\|^2 \right] dt.$$

Then, we proceed to analyze the sampling algorithm with choice 2. The ideal reverse process conditioned on  $\mathbf{c}_{1,s^*}$  and  $\mathbf{c}_{2,s^*}$  is given by,

$$\begin{aligned} d\mathbf{x}_{t,s^*} &= \left( \frac{\beta_t}{2} \mathbf{x}_{t,s^*} + \frac{\beta_t}{2} \nabla \log p(\mathbf{x}_{t,s^*} | \mathbf{x}_{0,1:s_{\text{ct}}}, \mathbf{c}_{1,s^*}, \mathbf{c}_{2,s^*}) \right) dt \\ &= \left( \frac{\beta_t}{2} \mathbf{x}_{t,s^*} + \frac{\beta_t}{2} \nabla \log p(\mathbf{x}_{t,s^*} | \mathbf{x}_{0,1:s_{\text{ct}}}, \mathbf{c}_{1,s^*}) + \frac{\beta_t}{2} \nabla \log p(\mathbf{c}_{2,s^*} | \mathbf{x}_{t,s^*}, \mathbf{c}_{1,s^*}) \right) dt. \end{aligned} \quad (32)$$

The corresponding Kolmogorov equation is given by,

$$\begin{aligned} & \frac{\partial}{\partial t} p(\mathbf{x}_{t,s^*} | \mathbf{x}_{0,1:s_{\text{ct}}}, \mathbf{c}_{1,s^*}, \mathbf{c}_{2,s^*}) \\ &= \nabla \cdot \left( p(\mathbf{x}_{t,s^*} | \mathbf{x}_{0,1:s_{\text{ct}}}, \mathbf{c}_{1,s^*}, \mathbf{c}_{2,s^*}) \left( \frac{\beta_t}{2} \mathbf{x} + \frac{\beta_t}{2} \nabla \log p(\mathbf{x}_{t,s^*} | \mathbf{x}_{0,1:s_{\text{ct}}}, \mathbf{c}_{1,s^*}) + \frac{\beta_t}{2} \nabla \log p(\mathbf{c}_{2,s^*} | \mathbf{x}_{t,s^*}, \mathbf{c}_{1,s^*}) \right) \right). \end{aligned}$$

Similarly, the continuous form of the approximate reverse process employed by choice 2 of the sampling algorithm is

$$d\mathbf{x}_{t,s^*} = \left( \frac{\beta_t}{2} \mathbf{x}_{t,s^*} - \frac{\beta_t}{2\sqrt{1-\bar{\alpha}_t}} \boldsymbol{\epsilon}_{\theta}(\mathbf{x}_{t,s^*}, \mathbf{x}_{0,1:s_{\text{ct}}}, \mathbf{c}_{1,s^*}) + \frac{\beta_t}{2} \mathbf{g}(\mathbf{x}_{0,1:s_{\text{ct}}}, \mathbf{c}_{1,s^*}, \mathbf{c}_{2,s^*}) \right) dt. \quad (33)$$

Its corresponding Kolmogorov equation is,

$$\begin{aligned} & \frac{\partial}{\partial t} q_{\theta}^{\text{ch}2}(\mathbf{x}_{t,s^*}) \\ &= \nabla \cdot \left( q_{\theta}^{\text{ch}2}(\mathbf{x}_{t,s^*}) \left( \frac{\beta_t}{2} \mathbf{x} + \frac{\beta_t}{2\sqrt{1-\bar{\alpha}}} \nabla \boldsymbol{\epsilon}_{\theta}(\mathbf{x}_{t,s^*}, \mathbf{x}_{0,1:s_{\text{ct}}}, \mathbf{c}_{1,s^*}) + \frac{\beta_t}{2} \nabla \mathbf{g}(\mathbf{x}_{0,1:s_{\text{ct}}}, \mathbf{c}_{1,s^*}, \mathbf{c}_{2,s^*}) \right) \right). \end{aligned}$$

Similarly, if we set  $\mu_1(\mathbf{x}_{t,s^*}) = \frac{\beta_t}{2} \mathbf{x}_{t,s^*} + \beta_t \nabla p(\mathbf{x}_{t,s^*} | \mathbf{x}_{0,1:s_{\text{ct}}}, \mathbf{c}_{1,s^*}) + \beta_t \nabla p(\mathbf{c}_{2,s^*} | \mathbf{x}_{t,s^*}, \mathbf{c}_{1,s^*})$  and  $\mu_2(\mathbf{x}_{t,s^*}) = \frac{\beta_t}{2} \mathbf{x}_{t,s^*} - \frac{\beta_t}{\sqrt{1-\bar{\alpha}_t}} \boldsymbol{\epsilon}_{\theta} + \beta_t \mathbf{g}$ , we can calculate  $L_1(r) \leq \frac{1+L_{\epsilon}+L_g}{2}$ . As a result, Lemma D.1 indicates

$$\begin{aligned} & \mathbf{W}_2 \left( p(\mathbf{x}_{0,s^*} | \mathbf{x}_{0,1:s_{\text{ct}}}, \mathbf{c}_{1,s^*}, \mathbf{c}_{2,s^*}), q_{\theta}^{\text{ch}2}(\mathbf{x}_{0,s^*}) \right) \\ & \leq \mathbf{W}_2 \left( p(\mathbf{x}_{T,s^*} | \mathbf{x}_{0,1:s_{\text{ct}}}, \mathbf{c}_{1,s^*}, \mathbf{c}_{2,s^*}), \mathcal{N}(0, \mathbf{I}) \right) \exp \left( T \frac{1+L_{\epsilon}+L_g}{2} \right) + \left( \int_0^T \exp(t(1+L_{\epsilon}+L_g)) \frac{\beta_t}{2} dt \right)^{\frac{1}{2}} \\ & \quad \times \sqrt{\frac{1}{2} \int_0^T \beta_t \mathbb{E}_{p_t(\mathbf{x}_{t,s^*})} \left[ \left\| \nabla p(\mathbf{x}_{t,s^*} | \mathbf{x}_{0,1:s_{\text{ct}}}, \mathbf{c}_{1,s^*}) + \frac{\boldsymbol{\epsilon}_{\theta}(\mathbf{x}_{t,s^*}, \mathbf{x}_{0,1:s_{\text{ct}}}, \mathbf{c}_{1,s^*})}{\sqrt{1-\bar{\alpha}}} + \nabla \log p(\mathbf{c}_{2,s^*} | \mathbf{x}_{t,s^*}, \mathbf{c}_{1,s^*}) - \nabla \mathbf{g} \right\|^2 \right] dt}. \end{aligned}$$

From the inequality  $\|a + b\|^2 \leq 2\|a\|^2 + 2\|b\|^2$ , we have,

$$\begin{aligned} & \left\| \nabla p(\mathbf{x}_{t,s^*} | \mathbf{x}_{0,1:s_{ct}}, \mathbf{c}_{1,s^*}) + \frac{\boldsymbol{\epsilon}_\theta(\mathbf{x}_{t,s^*}, \mathbf{x}_{0,1:s_{ct}}, \mathbf{c}_{1,s^*})}{\sqrt{1-\bar{\alpha}}} + \nabla \log p(\mathbf{c}_{2,s^*} | \mathbf{x}_{t,s^*}, \mathbf{c}_{1,s^*}) - \nabla \mathbf{g} \right\|^2 \\ & \leq 2 \left\| \nabla p(\mathbf{x}_{t,s^*} | \mathbf{x}_{0,1:s_{ct}}, \mathbf{c}_{1,s^*}) + \frac{1}{\sqrt{1-\bar{\alpha}}} \boldsymbol{\epsilon}_\theta(\mathbf{x}_{t,s^*}, \mathbf{x}_{0,1:s_{ct}}, \mathbf{c}_{1,s^*}) \right\|^2 + 2 \|\nabla p(\mathbf{c}_{2,s^*} | \mathbf{x}_{t,s^*}, \mathbf{c}_{1,s^*}) - \mathbf{g}\|^2. \end{aligned}$$

Combining them, we know

$$\begin{aligned} & \mathbb{W}_2 \left( p(\mathbf{x}_{0,s^*} | \mathbf{x}_{0,1:s_{ct}}, \mathbf{c}_{1,s^*}, \mathbf{c}_{2,s^*}), q_\theta^{\text{ch}^2}(\mathbf{x}_{0,s^*}) \right) \\ & \leq \mathbb{W}_2 \left( p(\mathbf{x}_{T,s^*} | \mathbf{x}_{0,1:s_{ct}}, \mathbf{c}_{1,s^*}, \mathbf{c}_{2,s^*}), \mathcal{N}(0, \mathbf{I}) \exp \left( T \frac{1 + L_\epsilon + L_g}{2} \right) \right) \\ & \quad + \left( \int_0^T \exp(t(1 + L_\epsilon + L_g)) \frac{\beta_t}{2} dt \right)^{\frac{1}{2}} \times \sqrt{2\mathcal{L}_1 + 2\mathcal{L}_2}, \end{aligned}$$

where  $\mathcal{L}_2$  is defined as,

$$\mathcal{L}_2 = \frac{1}{2} \int_0^T \beta_t \mathbb{E}_{p_t(\mathbf{x}_{t,s^*})} \left[ \|\nabla p(\mathbf{x}_{t,s^*} | \mathbf{x}_{0,1:s_{ct}}, \mathbf{c}_{1,s^*}) - \mathbf{g}(\mathbf{x}_{0,1:s_{ct}}, \mathbf{c}_{1,s^*}, \mathbf{c}_{2,s^*})\|^2 \right] dt.$$

This completes our proof. □